Study of microstructural, magnetic and electrical transport properties in YBCO/FePd heterostructures

Project thesis of

Mengying Tang

at the Jülich Centre for Neutron Science, Institute of Quantum Materials
and Collective Phenomena
in Forschungszentrum Jülich

supervised by
Prof. Dr. Thomas Brückel
Prof. Dr. Joachim Mayer

Dr. Emmanuel Kentzinger
Dr. Connie Bednarski-Meinke
Prof. Dr. Micheal Faley

01. October 2021 – 31. July 2022

Abstract:

The superconducting and ferromagnetic phases are fundamental and are direct macroscopic manifestations of many-body quantum physics. However, these two phases are largely incompatible. Furthermore, the interaction between superconducting and magnetic-order parameters at the mesoscopic length scale may lead to new physical phenomena [1, 2, 3].

In this article we will present the important features of hybrid superconductor(S)/ ferromagnetic(F) systems, more precisely YBCO/FePd heterostructures, such as the microstructure, magnetization and electrical transport properties and a comparison with ferromagnetic thin films. Our samples were produced by a combination of high oxygen pressure sputtering (HOPS) system and ultra-high vacuum molecular beam epitaxy (MBE). The samples' structural, magnetic and electrical transport properties were characterized by in-house techniques, such as, X-ray diffraction, magnetic force microscopy, magnetometry and resistivity. For both groups of samples, epitaxial growth on the MgO substrate was achieved with good quality. However, when FePd is deposited on YBCO, the FePd is shown to be polycrystalline from the RHEED pattern. FePd on MgO shows good perpendicular magnetic anisotropy with maze domain pattern, while the FePd on YBCO group does not show any magnetic domain pattern in out-of-plane direction. In the electrical transport measurements, the degradation of YBCO with the increase of FePd deposition temperature leads to the loss of superconductivity.

1 Introduction

Based on Dr. Annika Stellhorn's results, domain wall superconductivity and spin-triplet Cooper pair generation with large penetration depth in the ferromagnet in Ferromagnet(FePd) /Superconductor(Nb) heterostructures for quantum computing and spintronics device development is very favorable [1]. Hence, it can also be expected that a similar equivalent structure can be created by replacing Nb with a high temperature superconductor (HTS) such as $YBa_2Cu_3O_{7-\delta}$(YBCO) superconductor. The HTS/F heterostructure contributes to the current fundamental research on S/F proximity effects and this has also a great potential for the development of superconducting spintronic devices.

The perovskite YBCO's in-plane lattice constants of a=3.823Å and b=3.88Å are in good match with the tP4 unit cell lattice constants of FePd with a=b=3.849Å. In order to successfully grow hybrid YBCO/FePd (HTS/F) film, a heterostructure system of FePd/$YBa_2Cu_3O_{7-\delta}$/STO/MgO is proposed. Moreover, the superconducting state of YBCO is highly sensitive to its oxidation state, so immediate transfer is required to avoid impurities as well as superconducting failure.

The present study aims to investigate the electrical transport properties as a function of temperature and applied magnetic field in the epitaxial thin film heterostructures of HTS/F system $YBa_2Cu_3O_{7-\delta}$ /FePd, as well as the magnetic domain structure within the FePd layers.

2 Theroy

2.1 Ferromagnetism

Small magnetic domains (about 70 nm) can be observed by magnetic force microscopy in ordered FePd films, which are grown by molecular beam epitaxy. These films have perpendicular magnetic anisotropy. Thin films with magnetic properties having high perpendicular anisotropy are an efficient and attractive solution to increase the information density in magneto-optical recording media [4].

In this section, the basics of ferromagnetism, magnetic domain and magnetic anisotropy are discussed.

2.1.1 The Basics of Ferromagnetism

In the absence of an applied magnetic field, ferromagnetic materials still exhibit spontaneous magnetization, which is due to exchange interactions between electrons. The Heisenberg model is a useful model for describing the exchange interactions between spins, so ferromagnetism can be well modeled by using the Heisenberg model. The Hamiltonian of the Heisenberg model with an external applied magnetic field $\mu_0 \vec{H}_{ext}$ is given by (2.1):

$$\mathcal{H} = -\sum_{i,j} J_{i,j} \vec{S_i} \cdot \vec{S_j} + g\mu_B \sum_{j} \vec{S_j} \cdot \mu_0 \vec{H}_{ext} \tag{2.1}$$

Here, there is a reasonable assumption that a spin on site i will only interact directly with a neighboring spin, but not with the spin that is very far away. $J_{i,j}$ is the exchange coupling constant between the spins on sites i and j. In ferromagnetic materials, the electron spins tend to align in parallel, so $J_{i,j} > 0$. g is the Landé factor, and μ_B is the Bohr magneton.

When ferromagnetic materials are exposed to an external magnetic field, they will be highly magnetized in a direction parallel to the external magnetic field. If the external magnetic field is withdrawn, ferromagnetic materials also remain magnetized for a period of time. This phenomenon is called hysteresis. Hysteresis is a characteristic of ferromagnetic materials. Figure 2.1 shows the hysteresis characteristics of a typical ferromagnet.

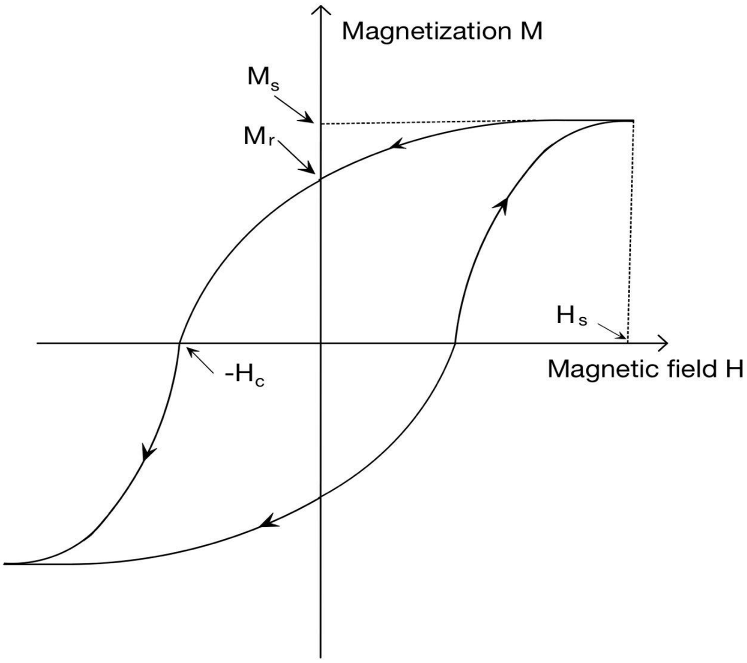

Figure 2.1: Magnetic hysteresis loop of a ferromagnetic material.

As the strength of the applied magnetic field increases, the magnetization strength also increases, but in a nonlinear manner, until the saturation magnetization strength M_s is reached. When the applied magnetic field is bigger than H_s, the continued increase in the applied magnetic field does not change the magnetization strength, because all the magnetic moments inside the ferromagnet are already aligned in a direction parallel to the external magnetic field. When the magnetic field decreases from positive to zero, the material still has some remaining magnetization strength M_r. In order for the magnetization strength to become zero, the magnetic field must increase in the opposite direction, the critical field necessary for this is called the coercive field H_c of the ferromagnet [5].

2.1.2 Magnetic Domain

The hysteresis of a ferromagnet is due to the existence of magnetic domains. The local magnetization in every tiny magnetic domain is saturated. The formation of "domain walls" separates these domains.

The magnetization in different magnetic domains is normally along different directions. When the applied magnetic field is 0, there is still some macroscopic residual magnetization, because there are some magnetic domains whose magnetization orientation cannot be canceled.

The macroscopic magnetization obtained at the coercive field is zero, because the magnetization directions of each magnetic domain are random, so these magnetization directions appear to cancel each other on the macroscopic scale. When the applied magnetic field is greater than H_s, the magnetic moments of all magnetic domains are aligned along the direction of the external magnetic field, and the magnetization at this time is the saturation magnetization M_s.

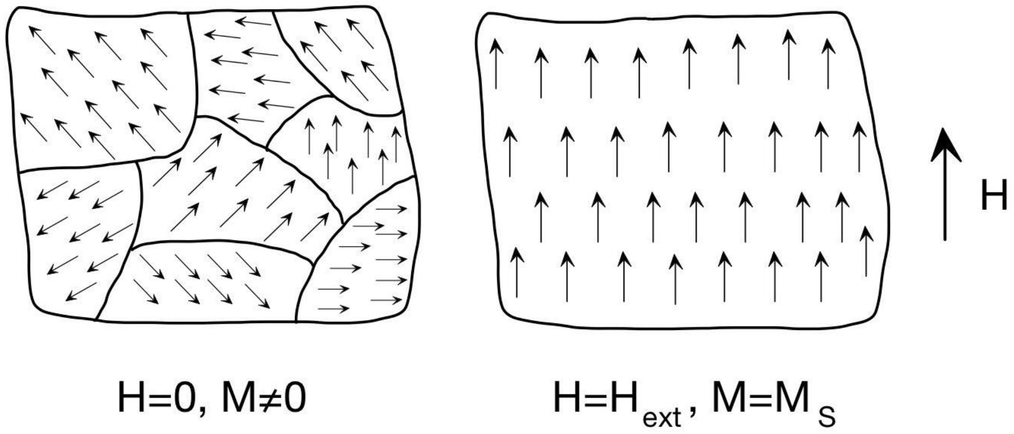

Figure 2.2: The magnetic domains and the spin orientations in zero (left) and external applied magnetic field H (right).

As shown in Fig. 2.3 (a) starting from the single domain state, (b)-(d) the domain walls start to be formed gradually and the total magnetic energy of the film is also gradually decreasing. The final size and shape of the magnetic domains are determined by the competition between the static magnetic energy and anisotropy.

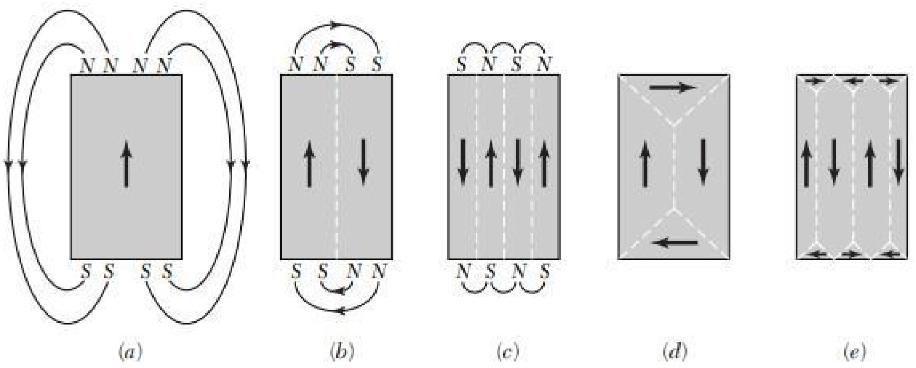

Figure 2.3: The origin of magnetic domains due to magnetostatic energy. The figure is adapted from [5].

2.1.3 Magnetic Anisotropy

Magnetic anisotropy in a ferromagnetic material is the existence of a specific direction in that material, along which the material can be easily magnetized, which is also known as the easy magnetization axis of the material.

There are three different sources of magnetic anisotropy, which are magnetic crystal anisotropy (E_{ma}), shape anisotropy (E_s) and magnetoelastic anisotropy (E_{me}).

2.1.3.1 Magnetocrystalline anisotropy

Electron spin is associated with orbital angular momentum via spin-orbit coupling. In the lattice, the orbital angular momentum is affected by the electrostatic potential of the lattice. This leads to an energetic preference of the orbital angular momentum for some crystal axes over others, and this asymmetry is transferred to the corresponding crystal axis. Thus, the magnetocrystalline anisotropy is related to the symmetry of the crystal.

2.1.3.2 Shape anisotropy

The shape anisotropy arises mainly from the demagnetizing field H_d, which is caused by the internal magnetization distribution. The geometry and size of the ferromagnetic sample determine the long-range dipole interactions. Shape anisotropy becomes particularly important in thin film samples. The shape anisotropy energy of thin film system is given by (2.2).

$$E_{sh} = \frac{1}{2}\mu_0 M_s^2 cos^2\theta \tag{2.2}$$

With M_s being the saturation magnetization and θ as the angle between the magnetization and the normal plane [6].

2.1.3.3 Magnetoelastic anisotropy

The shape or size of a ferromagnetic material changes, when an external magnetic field is applied. This effect is known as magnetostriction. On the contrary, if a stress is applied to the material, a change in the magnetization is induced, which is usually referred to as "inverse-magnetostriction" [7]. This magnetoelastic anisotropy caused by inverse-magnetostriction is associated with the magnetocrystalline anisotropy. The magnetoelastic anisotropy of crystalline thin film depends on the orientation between the applied strain and the crystal axes.

2.2 Superconductivity

In 1911 at the Leiden laboratory, when H. Kamerlingh-Onnes did his experiments to study the temperature dependence of the resistivity of mercury, he found that the resistance suddenly dropped to zero at temperatures T* close to 4K. Importantly, the resistance disappears immediately as the temperature decreases, rather than gradually. At low temperatures, the resistance is suddenly characterized by zero electrical resistance, this phenomenon is known as "superconductivity" [8].

In this section, the properties of superconductivity, as well as the most important theoretical models describing superconductivity will be outlined.

2.2.1 Properties of superconductivity

2.2.1.1 Perfect conductivity

As the temperature decreases, the resistivity of ordinary conductors such as silver and copper decreases gradually, but not infinitely. Some residual resistance also occurs. However, when superconductors such as Sn and Nb are cooled below a specific temperature, their resistance suddenly drops to zero. This phenomenon is known as perfect conductivity.

As shown in Figure 2.4 (a), the superconductivity transition temperature (or critical temperature, T_c) is the temperature that corresponds to when the resistance suddenly drops to 0. Superconductivity can be destroyed by heating ($T>T_c$) and also by applying an external magnetic field (the critical field of H_{cm}). H_{cm} is temperature dependent and can be described by (2.3):

$$\mathrm{H_{cm}} = \mathrm{H_{cm}}(0)\left[1-(\frac{\mathrm{T}}{\mathrm{T_c}})^2\right] \tag{2.3}$$

2.2.1.2 Perfect diamagnetism

When the temperature drops below T_c, the magnetic field inside the Superconductor will be excluded with or without the applied magnetic field ($H_{ext}<H_{cm}$), which is known as the Meissner-Ochsenfeld effect [8].

This shows that ideal diamagnetism is an intrinsic property of the superconducting state. At the same time, it proves that the superconducting transition is a phase transition.

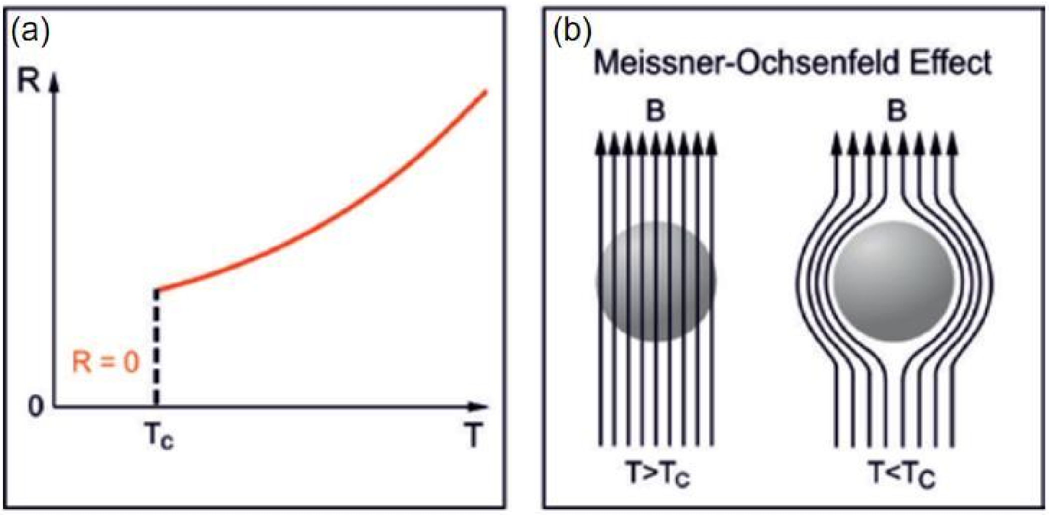

Figure 2.4: Properties of superconductivity. (a)Zero resistance (perfect conductivity). For $T < T_c$, superconductor has a perfect conductivity with zero resistance. (b) Meissner-Ochsenfeld effect (ideal diamagnetism). When temperatures $T > T_c$, the magnetic field B penetrates the superconductor, whereas for $T < T_c$, the magnetic field B is excluded from the superconductor. The figure is adapted from [9].

2.2.1.3 Type-II superconductors

Superconductors can be divided into two types according to the different states they show in response to external magnetic fields.

Type-I superconductors, which have perfect diamagnetism when the applied magnetic field is less than H_{cm}.

Type-II superconductors, including Nb, superconducting alloys and compounds, exhibit perfect diamagnetism only when the applied magnetic field is lower than the lower critical magnetic field H_{c1}.

When H is higher than H_{c1} and lower than the upper critical magnetic field H_{c2}, the superconductor is in the mixed state. At this intermediate state, the magnetic field can penetrate the superconductor in the form of quantized vortex (Figure 2.5). Each vortex carries a single magnetic flux quantum of Φ_0. As the external magnetic field increases, more and more quantized vortices appear. When the density of vortices is high enough for $H>H_{c2}$, the superconductivity is broken.

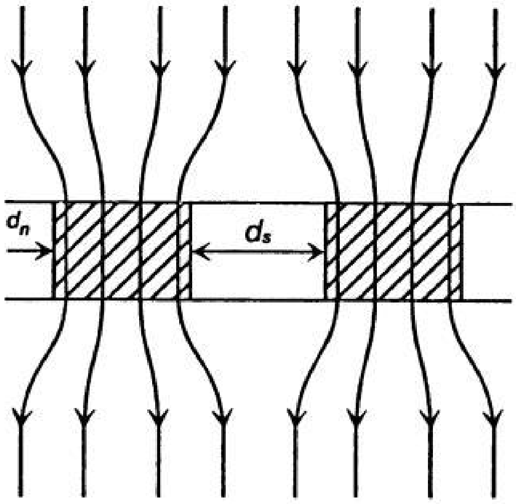

Figure 2.5: Intermediate state (mixed state) of a thin superconducting layer with a perpendicular field; With d_s being the width of a superconducting region and d_n as the width of a normal region. The figure is adapted from [8].

2.2.2 BCS theory

The BCS theory is a microscopic theory that explains the superconductivity of conventional superconductors. The theory is named after J. Bardeen, L.V. Cooper and J.R. Schrieffer.

In BCS theory, electrons move through the lattice and attract a positive charge from neighbouring lattice points at the same time. Which causes a local deformation of the lattice point, resulting in a localized region of high positive charge. This localized region of high positive charge in turn attracts electrons of opposite spin and momentum. The electrons are then paired with the original electrons with a certain binding energy. When temperature is lower than critical temperature, this binding energy may be higher than the energy of the lattice atomic vibration. Therefore, the electron pair does not exchange energy with the lattice and there is no resistance, forming what is known as "superconductivity". The mutual attraction between electrons is indirectly caused by the interaction between electron and lattice vibrations (phonons). Two electrons with opposite spin and momentum are coupled at $T < T_c$ and then form a Cooper pair (CP).

2.2.3 Ginzburg-Landau theory

In Ginzburg-Landau theory (G-L theory), Ginzburg and Landau decided to consider an effective wavefunction of the superconducting electrons $\Psi(\mathrm{r})$ as an order parameter. The macroscopic wave function can be described by the local density of Cooper pairs (CPs):

$$|\Psi|^2 = \frac{n_s}{2} \tag{2.4}$$

With n_s being the local density of the superconducting electrons.

The expansion of free energy F of a superconducting condensate is given by:

$$F = F_n + \alpha|\Psi|^2 + \frac{\beta}{2}|\Psi|^4 + \frac{1}{2m^*}\left|-i\hbar\nabla\Psi - \frac{2e}{c}A\Psi\right|^2 + \frac{H^2}{8\pi} \tag{2.5}$$

With the free energy in the normal state F_n, the electron mass m, charge e, the magnetic energy density $H^2/8\pi$, the exact microscopic field at a given point of the superconductor H. The forth term is the kinetic energy density of the superconducting electrons [8].

By calculating $\boldsymbol{j}_s = -\delta F[\Psi, A]/\delta A(r)$, the second equation of Ginzburg-Landau theory can be obtained:

$$\boldsymbol{j}_s = -\frac{i\hbar e}{2m}(\Psi^*\nabla\Psi - \Psi\nabla\Psi^*) - \frac{2e^2}{mc}|\Psi|^2\mathbf{A} \tag{2.6}$$

Where A is the vector potential, $\boldsymbol{j}_s$ is the current density in the superconductor. In addition, with Maxwell's equation and ${\Psi_0}^2 = n_s/2 = |\alpha|/\beta$, two more definitions will be introduced [8]:

Coherence length ξ describes the correlation length between two electrons of a Cooper pair in a superconductor, in other words, the distance that the Cooper electron pair extends in space.

$$\xi = \sqrt{\frac{\hbar^2}{4m|\alpha|}} \tag{2.7}$$

The London penetration depth is the depth at which the magnetic field penetrates into the superconductor and the field strength diminishes to 1/e of the strength at the surface of the superconductor. Penetration depth λ for a weak magnetic field [8]:

$$\lambda = \sqrt{\frac{\mathrm{m}c^2\beta}{8\pi e^2|\alpha|}} \tag{2.8}$$

Both coherence length ξ and penetration depth λ are temperature dependent [8].

When the temperature is close to T_c:

$$|\alpha| \propto (T_c - T) \tag{2.9a}$$

Therefore:

$$\xi, \lambda \propto (T_c - T)^{-1/2} \tag{2.9b}$$

2.2.4 High Temperature Superconductors

Although there is still no clear theory to explain their high critical temperatures, high-temperature superconductors are still superconductors and they have both a Meissner state and an intermediate state [8]. The BCS theory can describe the conductivity mechanism of ordinary superconductors well, however, it cannot explain high-temperature superconductors.

In classical superconductors, the mobile charges are Cooper pairs with two negative charges. However, in a high temperature superconductor like YBCO, it is better to consider the Cooper pairs as hole pairs rather than electrons [11]. The crystal is a stacked sequence of CuO_2 planes alternating with other oxide layers [8]. It is similar to perovskite with a unit cell consisting of stacked $BaCuO_3$ and $YCuO_3$ cubes as shown in Figure 2.6. There are two copper-oxygen planes in this structure, the first one is above and below the yttrium atom, and there are two oxygen atoms per copper (CuO_2) in this plane, while there is one copper (CuO) per oxygen in the other plane. These CuO planes are called oxygen-deficient planes. The superconductivity of high-temperature superconductors of the YBCO system probably comes from these copper oxide layers, since they are common to copper oxide superconductors. The amount of oxygen in the copper oxide planes can change the ratio of Cu^{2+} to Cu^{3+}. The ratio of these two states Cu^{2+} and Cu^{3+} affects the number of holes. The superconducting state depends on the concentration of holes. Therefore, changing the oxygen content in YBCO will change the critical temperature [30].

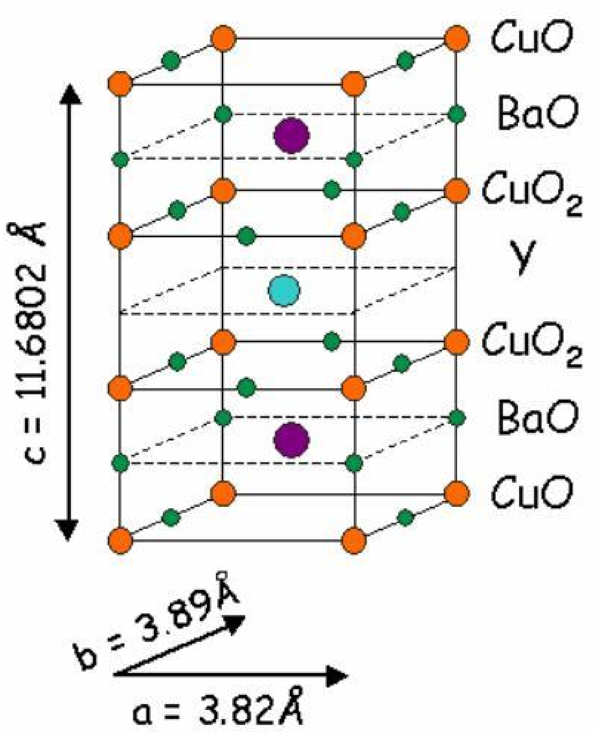

Figure 2.6: Schematic structure and chemical composition of YBCO, taken from [11].

2.3 Domain superconductivity

For S/F systems with ferromagnetic layers having a magnetic domain structure, where the magnetic field acts only on a small region at the S/F interface, the previously homogeneous superconducting state in the S film can be confined to the small region by the orbital pair breaking effect [1]. Superconductivity will preferentially nuclei at the minimum magnetic field strength. This magnetic field strength is determined by both the applied magnetic field and the stray field [2]. In this subsection, the cases of no applied magnetic field and with applied magnetic field are discussed separately.

2.3.1 Domain-wall Superconductivity (DWS)

As shown in Figure 2.7 right, the superconducting film layer is deposited on top of the ferromagnetic film layer. The easy magnetization axis of ferromagnetic film is in the direction along the z-axis. At this point, the distribution of the stray field within the superconducting layer is almost uniform.

Within the left panel of Figure 2.7, the red line represents the stray field distribution within the superconducting layer. The temperature is now gradually reduced to T_c and the superconductivity of the superconducting layer appears.

In the absence of an applied electric field, the Cooper pair preferentially nucleates at the lowest stray field, more precisely, when the magnetic field in this region is less than upper critical field H_{c2}. Corresponding to the right diagram in Figure 2.7, superconductivity appears above the domain wall [2].

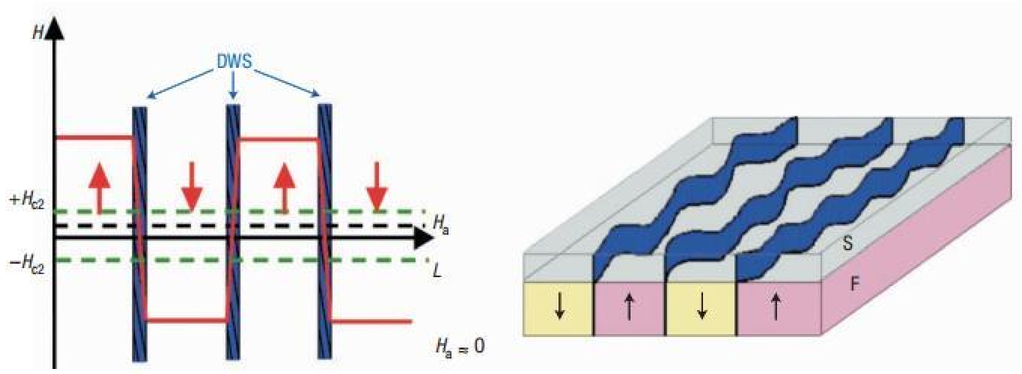

Figure.2.7: Schematic illustrations of domain-wall superconductivity (DWS) in superconductor/ferromagnet thin film system.The figure is adapted from [2].

2.3.2 Reverse-domain Superconductivity (RDS)

When an external magnetic field is applied perpendicular to the film and oriented upwards and the magnitude of the applied field equals to the saturation field H_s, this results in the magnetic field above the reversed domain being fully compensated. In this case, the Cooper pairs have more tendency to nucleate above the reversed domain.

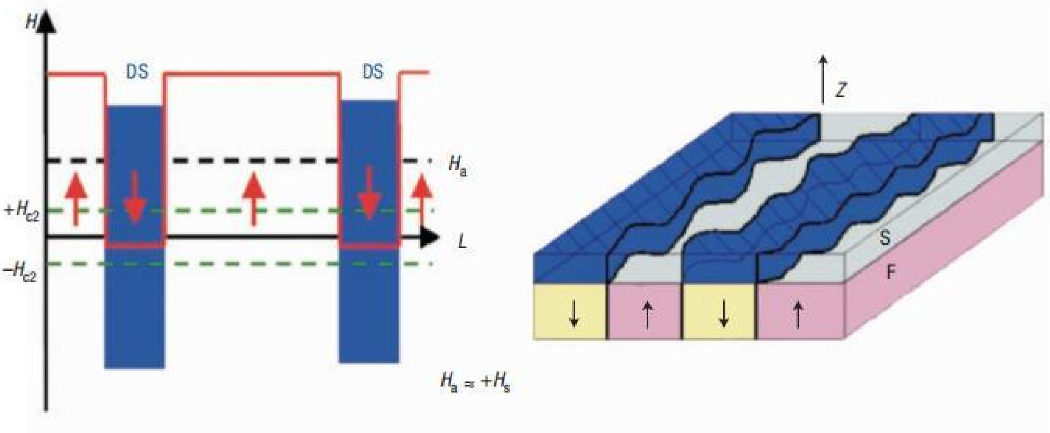

Figure 2.8: Schematic illustrations of reverse-domain superconductivity (RDS) in superconductor/ferromagnet thin film system. The figure is adapted from [2].

3 Experimental Methods

In this chapter, the principles and basic operation of the relevant experimental apparatus are briefly described. The FePd films in the F/S heterostructured films were grown in an oxide molecular beam epitaxy (OMBE) system. In the OMBE system, reflection high energy electron diffraction (RHEED) is the typical method for in-situ characterization to monitor the growth mode of films in real time. The out-of-plane structure of hybrid superconductor-ferromagnet (S/F) systems were determined by X-ray diffraction. This is followed by the obtaining topographic information of the film surface and the magnetic domain structure by using AFM and MFM, respectively. Finally, the magnetization-field (M-H) and resistance-temperature (R-T) curves were measured through magnetic property measurement system (MPMS) and physical property measurement system (PPMS) respectively.

3.1 Sample Preparation

3.1.1 Oxide Molecular Beam Epitaxy

Epitaxy is a technique for the preparation of single crystal thin films, which allows the film to be grown layer by layer in the direction of the crystallographic axis of the substrate material in suitable conditions. The advantages of this technique are: the growth rate of the film layer is slow, the precise control of the beam intensity can be realized, the layer components and doping concentrations can be adjusted rapidly in response to the changes from source. With this technique, ultra-thin layers of quantum microstructural materials can be formed by alternating the growth of films with different components.

As shown in Figure 3.1, the M600 OMBE system consist mainly of a load lock, a transfer line and a main chamber.

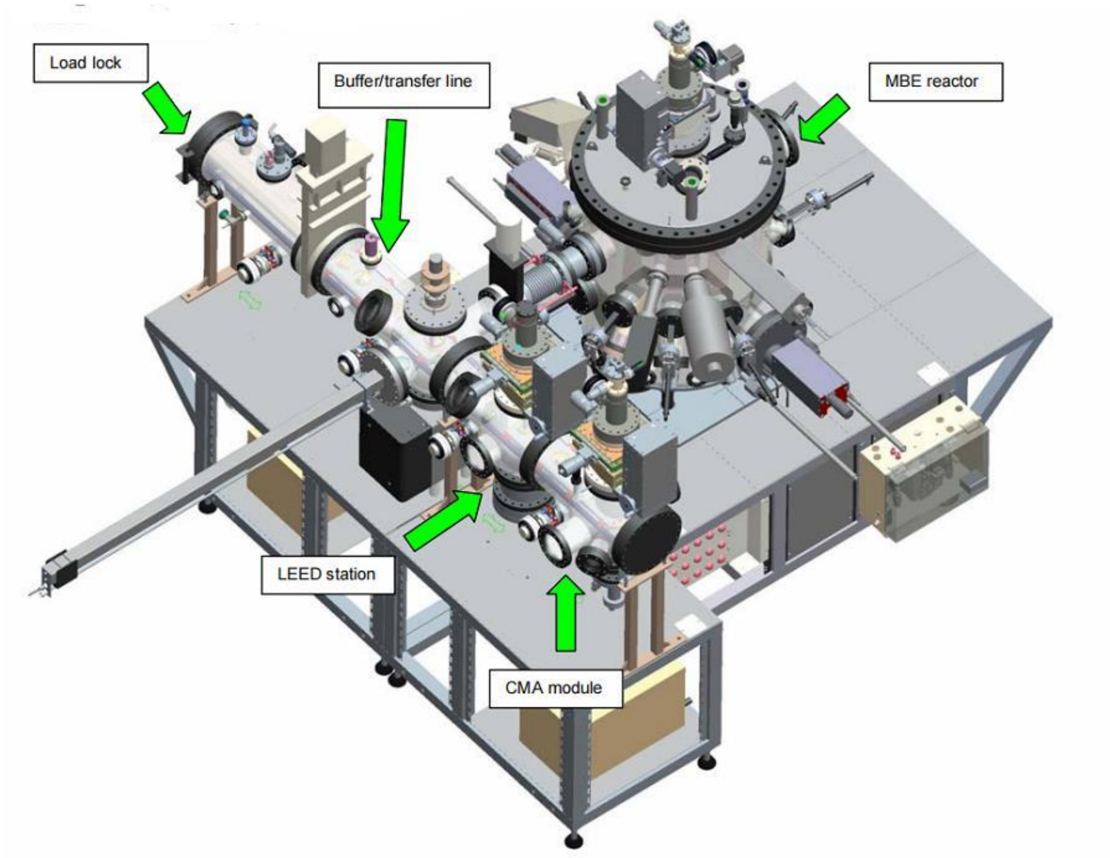

Figure 3.1: Layout of M600 MBE system.
This figure is adapted form [12].

After venting the load lock, the sample is loaded in a sample holder to the trolley in the load lock. Close the load lock and open the gate valve between the load lock and buffer line, when the pressure in the load lock is almost equal to the pressure in the buffer line. In the buffer line, the sample can be further transferred into the main chamber via the transfer arm.

As shown in Figure 3.2, there are shutters above each effusion cell, and the deposition time of different components can be flexibly controlled by the switch of the shutter, so that different growth modes (co-/shuttered-deposition) can be realized. Quartz crystal microbalance (QCB) can monitor the evaporation rates of individual components in real time before deposition begins. The evaporation rate of each component can be adjusted by raising or lowering the temperature of the corresponding Effusion cell.

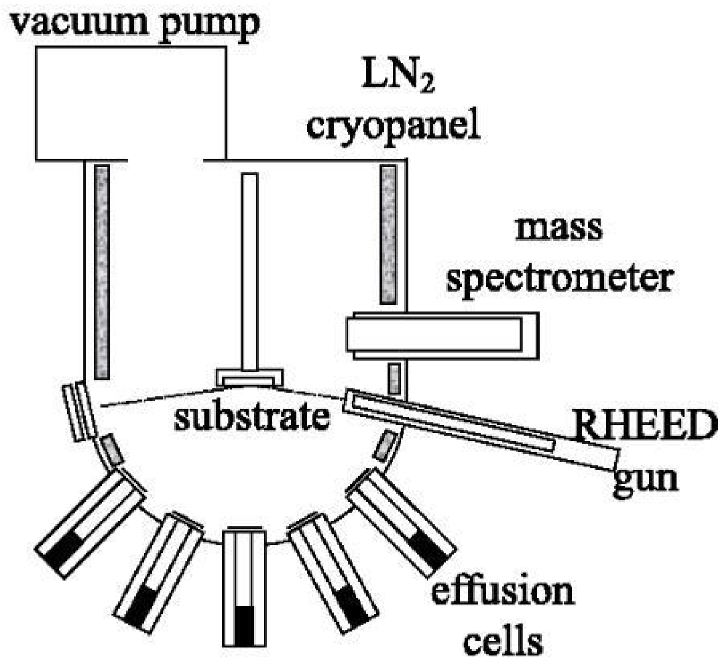

Figure 3.2: Schematic simplified cross section structure of the OMBE main chamber. This figure is taken from [31].

3.1.2 Reflection High Energy Electron Diffraction RHEED

RHEED is an essential in-situ characterization technique for molecular beam epitaxy systems, where the penetration depth of the RHEED electron beam is only 1 - 2 atomic layers and therefore the RHEED image shows the structural information of the sample surface at the atomic level. It allows diffraction investigations of the surface and growth monitoring during the growth of the film.

In this study, the RHEED system attached to the MBE equipment was used (Figure 3.2). Different RHEED images correspond to different surface structures, e.g. single crystal, polycrystalline, three-dimensional island structures, etc. If the film is grown layer by layer, as shown in Figure 3.3 (b), the specular beam intensity on the fluorescent screen oscillates. The intensity is highest when the film surface is very flat, i.e. 100% coverage. The intensity is lowest when the film surface is only 50% covered.

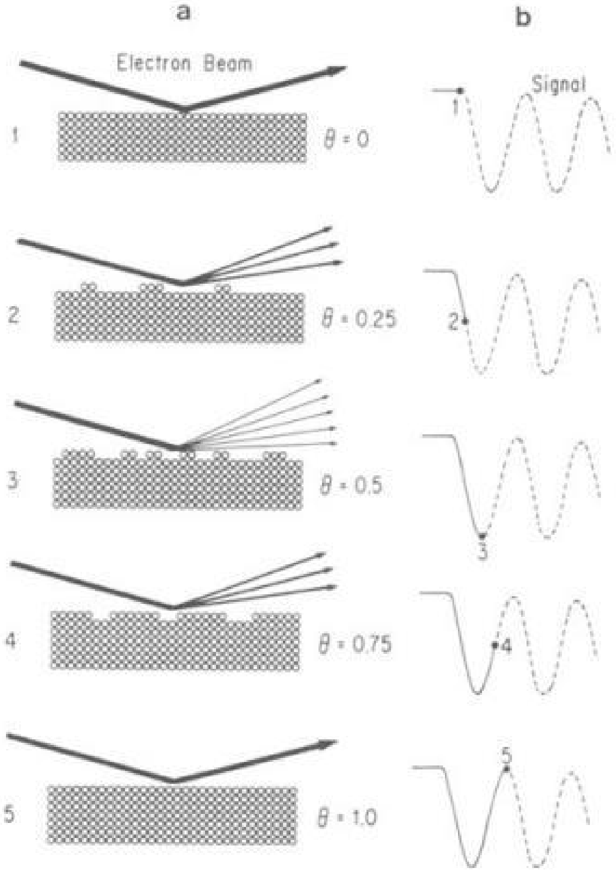

Figure 3.3: Model for RHEED intensity oscillations: (a) relationship between surface coverage and reflected electron beam; (b) beam intensity variation from RHEED screen. Taken from [14].

3.2 Characterization Methods

3.2.1 X-ray Diffractometer

As shown in Figure 3.4, the Bruker D8 Advance refractometer instrument consists of an X-ray tube (left), the sample stage (middle) and the detector (right) and can be used to analyse the out-of-plane crystallinity. The system uses an X-ray source with a wavelength of 1.54055 Å, corresponding to the $\mathrm{Cu} - \mathrm{K}_{\alpha 1}$ transition. A highly collimated beam is achieved by two Göbel mirrors in front of and behind the sample. Monochromatic beam selection is achieved by mounting a channel cut monochromator.

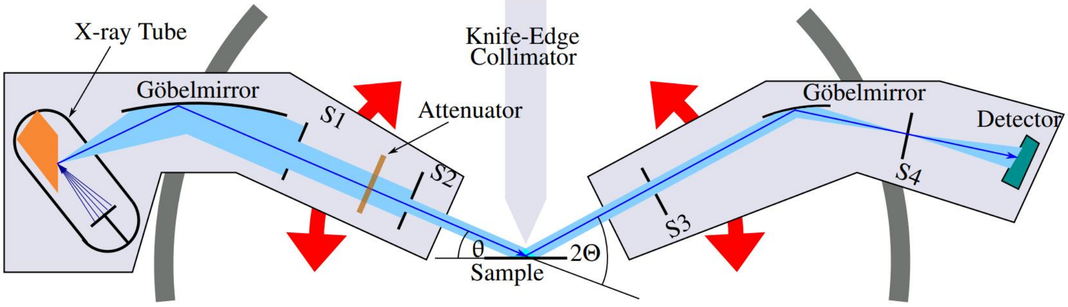

Figure 3.4: Schematic geometry of D8 X-ray Diffractometer, taken from [15].

3.2.2 Atomic Force Microscope and Magnetic Force Microscopy

Both surface topography and magnetic domain characterization can be achieved with the Agilent Technologies 5400 Atomic Force Microscope (AFM). The Agilent 5400 AFM system mainly consists of a magnetic sample stage, a scanner with a (magnetic) tip, a laser diode and detector, and a piezo system to control the cantilever.

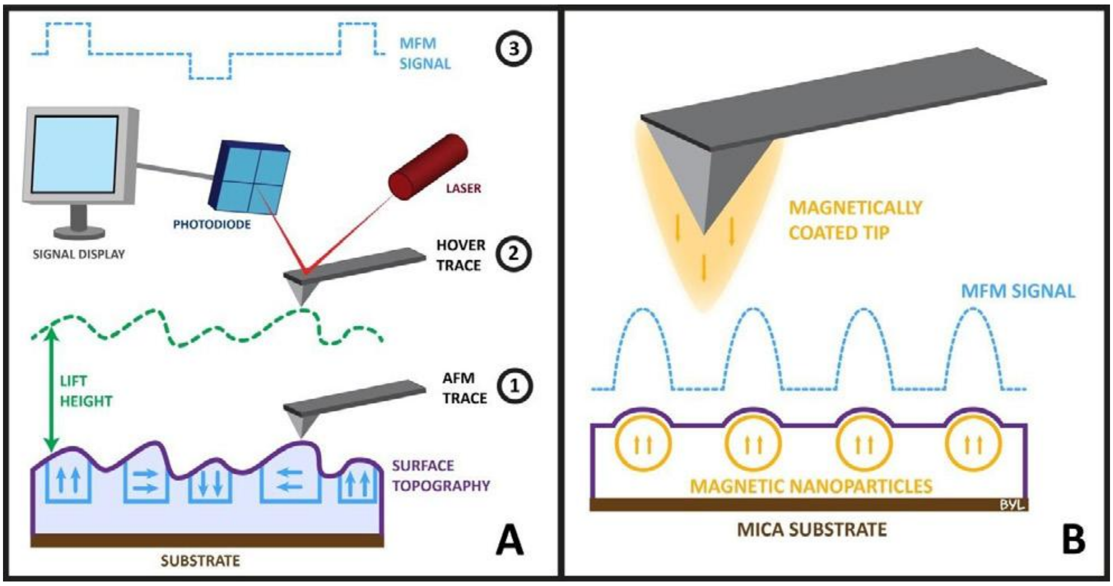

Figure 3.5: Schematic setup and principle of AFM (A) and MFM (B) imaging techniques, taken from [16].

In tapping mode, the feedback parameter is the cantilever oscillation amplitude. The movement of the cantilever probe is achieved by adjusting the z-piezo so that the feedback parameter keeps constant at the set value. The resulting z-piezo movements provides the height change from surface. The signal of the cantilever deflection is recorded by a laser beam reflected from the back of the cantilever onto a photodiode.

The AFM tip scans the surface of the sample to produce a topographic trajectory. In MFM, there are two scans: one across the topography and one at the pull-away distance. The cantilever beam is raised to a user-defined height away from the sample surface (pull-away distance), the sample surface is scanned using the magnetically coated tip and the tip moves along the topographic trace. The magnetic signal is recorded as the tip interacts with the magnetic domains in the sample.

3.2.3 Magnetic Property Measurement System

In this study, the magnetic properties of the samples were measured using the Magnetic Property Measurement System (MPMS) from Quantum Design Inc. (Fig.3.6). In the MPMS, the sample is mounted in a straw in a direction parallel or perpendicular to the magnetic field, respectively. It forms a second-order gradiometer together with a superconducting coil surrounding the outside. As the sample moves up and down through the coil, the local magnetic flux density varies with the motion of the sample. The change in magnetic flux can be measured using a liquid helium-cooled SQUID (superconducting quantum interference device).

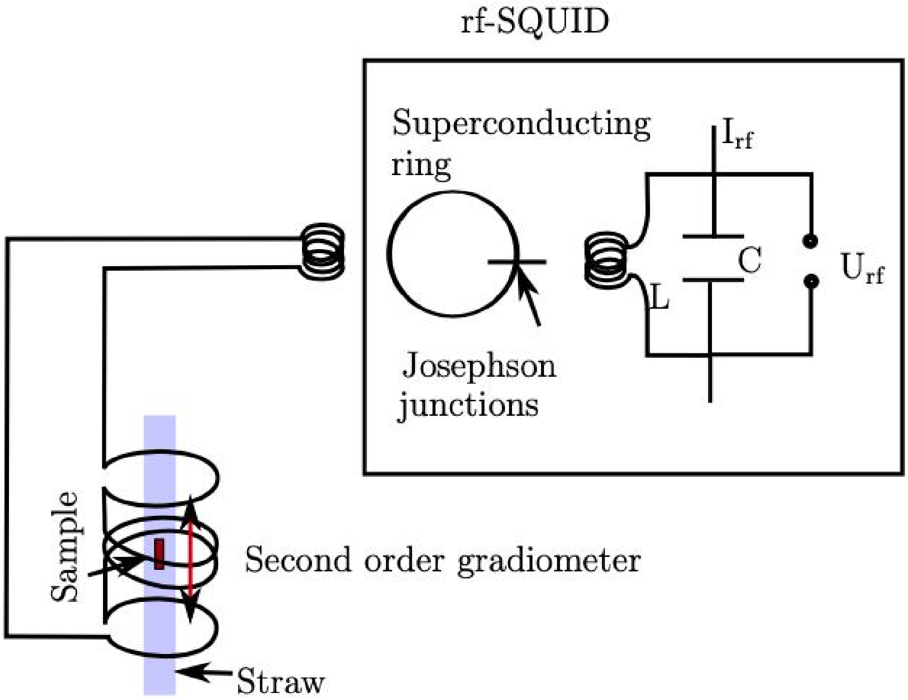

Figure 3.6: Schematic image of the principle of MPMS,taken from [18].

Using the Josephson effect, the SQUID can monitor very small changes in magnetic flux. Typically, SQUID is a superconductor ring, but it is interrupted by one or more Josephson junctions [17]. The voltage drop across the Josephson junctions changes as the externally varying magnetic flux is coupled to the Josephson loop. Combining the change in voltage with the motion of the sample determines the amount of flux coupled into the SQUID loop.

3.2.4 Physical Property Measurement System

The electrical transport properties of films are measured by the Quantum Design Dynacool-PPMS (Physical Property Measurement System). The electrical transport properties of hybrid superconductor-ferromagnet (S/F) films at different temperatures and applied magnetic fields are measured by Quantum Design Dynacool-PPMS (Physical Property Measurement System). The working temperature range of PPMS is from 1.9K to 400 K and the applied magnetic field can be as high as 9 Tesla. The AC current used in this experiment is 10 μA.

A thermometer and a heater are installed below the sample puck for precise temperature control. A superconducting solenoid valve is mounted around the main chamber, which can generate the required magnetic field. The electrical transport properties can be measured by using silver wires and indium to realize connection between the corresponding contact points on the puck and sample .

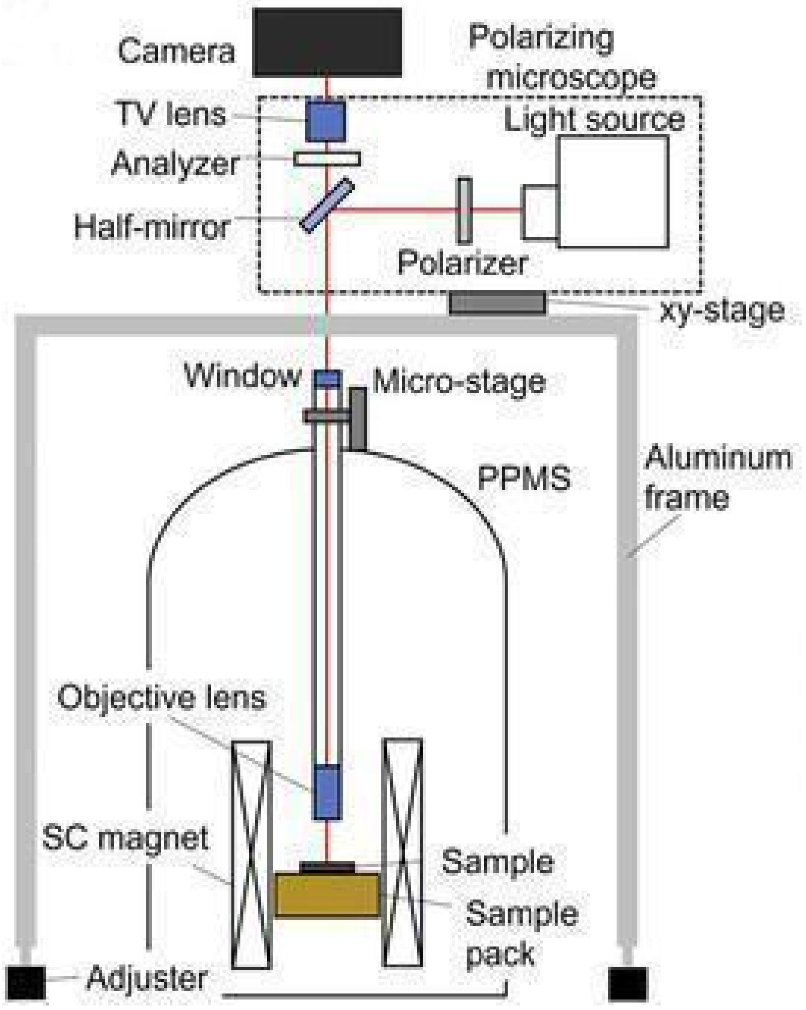

Figure 3.7: Schematic image of major components of the PPMS, this figure is taken from [19].

4 Result and Discussion

The main objective of this study is to investigate whether there is a proximity effect in the MBE-grown FePd/YBCO heterostructures. Therefore, a comparison group FePd/MgO was set up in this study to contrast with the experimental group samples with YBCO superconducting material. We refer to the FePd/MgO sample as the F group, while FePd/YBCO sample is referred to as the F/S group. For both thin film system, the microstructure, magnetic transport, and electrical transport properties of the samples can be specifically analyzed.

4.1 Sample preparation

OMBE is an excellent thin film epitaxial growth method which is accurate down to the atomic monolayer. Thus, OMBE is a good growth method for multilayer systems. It allows precise control and monitoring of the quality and interfacial conditions for each grown film [1]. The quality of the film can be controlled by adjusting the growth parameters, such as evaporation rate (effusion cell temperature), substrate temperature, growth mode (co-deposition/ shuttered deposition).

4.1.1 Substrate

The substrate MgO from CrysTec GmbH is one-side polished with lattice constant a=0.4212nm [20]. In order to get a good quality of the subsequently grown crystal epitaxial layers, the substrate was first blown off using nitrogen gas to remove dust, and then it was sent into the main chamber of the OMBE system under ultra-high vacuum, finally it was annealed at 450◦C for 1 hour then 550◦C for 10 minutes [21].

The flatness of the substrate surface can be analyzed by comparing the RHEED images shown in Figure 4.1. From the comparison of these two images, it can be easily noticed that the RHEED image of annealed MgO substrate exhibits a sharper Kikuchi line, which indicates that annealed sample has high crystalline order and annealing is effective in making the sample surface smoother.

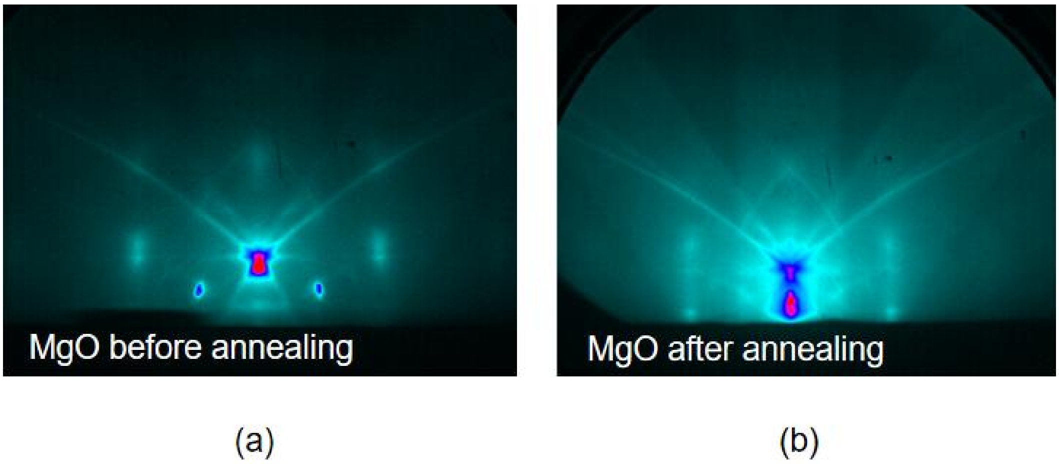

(a) (b)

Figure 4.1: The RHEED pattern of MgO substrate before and after annealing. Both patterns were taken in the same orientation (110).

4.1.2 Growth parameter

The film thicknesses and deposition rates for experiments were obtained from the optimized experimental data of Dr. Annika Stellhorn [1] and Prof. Dr. Michael Faley [22].

In this study, a total of seven different schemes of film were designed, as shown in the table 4.1 below.

Table 4.1 Sample list of comparison F group and F/S system group

sample	substrate	deposition method	deposition temperature	Thickness of FePd/nm
MgO/Pd/FePd (co, 230℃)	MgO	co	230℃	40
MgO/Pd/FePd (sh, RT)	MgO	shuttered	RT	40
Old YBCO/FePd (sh, RT)	MgO-YBCO	shuttered	RT	40
YBCO/Pd/FePd (sh, RT)	MgO-YBCO	shuttered	RT	40
YBCO/FePd (co, 150℃)	MgO-YBCO	co	150℃	40
YBCO/FePd (co, 230℃)	MgO-YBCO	co	230℃	40
New YBCO/FePd (sh, RT)	MgO-YBCO	shuttered	RT	20

The first two samples are the comparison F group and the rest of the samples are the F/S group. The sample to be mentioned here is Old YBCO/FePd (sh, RT), where old represents that there was a period of about 3 months between the deposition of YBCO and the deposition of FePd. YBCO sample was kept under vaccum in the buffer line of the OMBE system during this interval. After the deposition of YBCO, the rest of the samples were transferred immediately to the MBE main chamber for FePd deposition. For the last sample New YBCO/FePd (sh, RT), FePd was only 20 nm in order to make it easier to do TEM experiments.

In order to grow single-crystal films with high perpendicular magnetic anisotropy with suitable stoichiometric ratios, the growth rates of Fe and Pd were directly adopted from the optimal parameters in Dr. Annika Stellhorn's paper [1]. By varying the temperature of the effusion cells, the evaporation rate of the individual materials can be changed.

$$\mathrm{T} = \mathrm{Ct}\frac{\partial \mathrm{f}}{\partial \mathrm{t}} \tag{4.1}$$

where T is the thin film thickness, C is a constant, t is the growth time and $\partial \mathrm{f}/\partial \mathrm{t}$ is the change rate of the resonant frequency.

Since it is unrealistic to adjust the evaporation rate to be exactly the same as the optimized parameters, the following equation can be used to calculate the appropriate evaporation rate.

$$\mathrm{t_{new}} = \mathrm{t_{old}}\,\frac{\frac{\partial \mathrm{f}}{\partial \mathrm{t}_{\mathrm{old}}}}{\frac{\partial \mathrm{f}}{\partial \mathrm{t}_{\mathrm{new}}}} \tag{4.2}$$

Where $\mathrm{t_{old}}$, $\partial \mathrm{f}/\partial \mathrm{t_{old}}$ are optimized parameters, $\partial \mathrm{f}/\partial \mathrm{t_{new}}$ is change rate of the resonant frequency after adjustment in new experiments, $\mathrm{t_{new}}$ is the growth time that needs to be set in the program for new experiments.

4.1.3 Thin Film Growth

For comparison F group, a 60nm Pd buffer layer was first deposited on the annealed smooth substrate to alleviate the large mismatch (8.59%) between MgO and FePd. The Pd buffer layer reduced the lattice mismatch to 1.03%, effectively and significantly reducing the lattice mismatch and provided a good prerequisite for subsequent epitaxial growth. The Pd buffer layer was then annealed in 350 ℃ for 30 min to provide a uniform and flat surface.

Subsequently, FePd films with high and low PMA were deposited by using these two methods of co-deposition and shuttered-deposition growth, respectively. Co-deposition is a process where two materials are deposited on a surface simultaneously [21]. In the case of FePd films, it means opening the shutter above the Fe and Pd Knudsen cells at the same time, allowing Fe and Pd to be deposited on the Pd buffer layer at the same time. Shuttered deposition is the process of interleaved deposition of different materials' monolayers by controlling the opening and closing of the shutter above two or more Knudsen cells via the control program.

Finally, a thin Pd capping layer was deposited on top of the FePd layer to prevent FePd from being oxidized. Specific details of the growth parameters can be found in Table 4.2 below.

Table 4.2 Optimized growth parameters used for co-deposition and shuttered growth.

sample	t_{Pd} [s]	$-\partial f/\partial t_{Pd}$ [Hz/s]	t_{Fe} [s]	$-\partial f/\partial t_{Fe}$ [Hz/s]
MgO/Pd/FePd (co, 230℃)	5110	-0.382	5110	-0.176
MgO/Pd/FePd (sh, RT)	2310	-0.914	2090	-0.494
Old YBCO/FePd (sh, RT)	2310	-0.912	2090	-0.481
YBCO/Pd/FePd (sh, RT)	2310	-0.923	2090	-0.492
YBCO/FePd (co, 150℃)	2400	-0.814	2400	-0.375
YBCO/FePd (co, 230℃)	2410	-0.810	2410	-0.377

New YBCO/FePd (sh, RT)	2310	-0.915	2090	-0.493

The growth process is schematically shown in Figure 4.2.

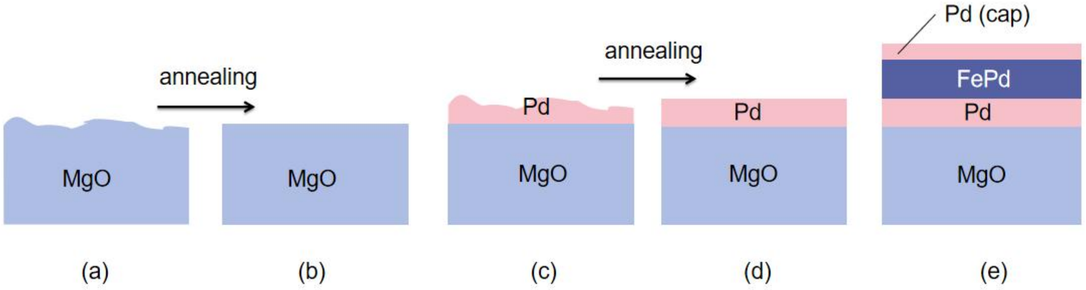

Figure 4.2: (a) Unannealed MgO substrate. (b) Annealed MgO substrate. (c) Pd buffer layer before annealing. (d) Pd buffer layer after annealing. (e) The final sample with a Pd capping layer.

For F/S system group, the YBCO thin film was made through high oxygen sputtering by Prof. Dr. Faley. At least two buffer layers are required to deposit YBCO on MgO: the first one should provide the epitaxial growth of films with perovskite structure on the rocksalt structure of MgO, so 3nm YBCO was first deposited on MgO as a seed layer. A buffer 20nm STO keeps the moisture-absorbing surface of the MgO substrates from degradation in air and/or during the lithographic procedures and the second buffer layer should match the lattice constants [23].

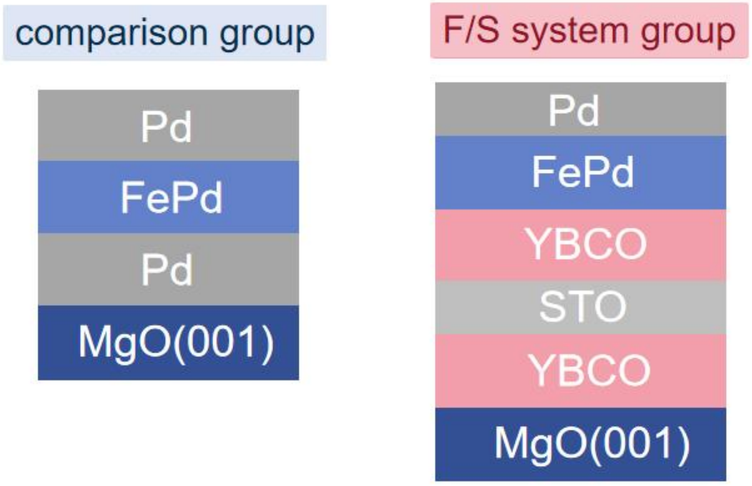

Figure 4.3: Schematic structure of F group and F/S system group.

The rest of the process is the same as group F. The FePd layer (with co-deposition and shuttered-deposition) and finally the Pd capping layer are deposited sequentially above the YBCO.

In contrast to the F group, there are subtle differences in the deposition of FePd in the F/S group. Because of the need to study the proximity effects, there cannot be a very thick buffer layer between YBCO and FePd layers. In the F/S group, only a 1 nm Pd buffer layer was deposited in sample YBCO/Pd/FePd (sh, RT), the rest samples had no Pd buffer layer. Since YBCO cannot withstand high temperatures in a high vacuum anaerobic environment, we experimented with lowering the deposition temperature here, i.e., from 230℃to 150℃, to prevent YBCO degradation.

4.1.4 Reflection High-Energy Electron Diffraction

Reflection high-energy electron diffraction (RHEED) is a technique used to characterize the surface of crystalline materials. For the multilayer thin film system in this study, in-situ characterization of RHEED plays a really important role. During the growth of the film, RHEED can monitor the growth mode of each layer in real time, and the surface roughness and surface reconstruction can be also qualitatively checked from RHEED images.

4.1.4.1 Comparison F Group

Figure 4.4 shows the RHEED patterns of sample MgO/Pd/FePd (co, 230°C) in (110) direction during the FePd deposition.

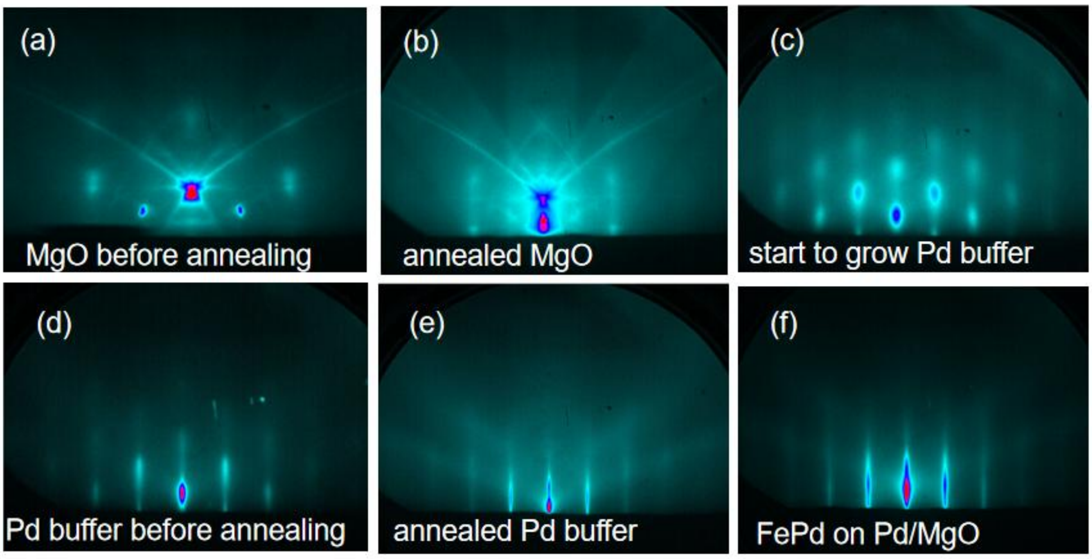

Figure 4.4: RHEED patterns of comparison F group in (110) crystallographic direction. (a) MgO substrate before annealing. (b) Annealed MgO substrate with flat surface and high crystalline order. (c) RHEED pattern was taken when Pd buffer layer was started to grown. (d) Pd buffer layer before annealing (e) Annealed Pd buffer layer showed Kikuchi lines. (f) Patterns of FePd layer.

The Kikuchi lines can be seen in Figure 4.4(a) on the MgO substrate even before annealing, which indicates that the polished MgO substrate itself was flat. After the MgO substrate was annealed, the Kikuchi lines were more pronounced and sharp, which means that the annealing has homogenized the surface and made it smoother.

Just when the shutter of Pd Knudsen cell was opened in preparation for depositing the Pd buffer layer, the RHEED pattern showed some bright spots in Figure 4.4(c), which represents that Pd is currently growing in an island growth mode. When the surface is rough with three-dimensional island as shown in Figure 4.5(c) and the glancing angle of the electron beam is small, the electron beam will transmit through the island protrusion. The pattern produced on the fluorescent screen at this time is a transmission diffraction pattern instead of a reflection pattern [24].

When the deposition of the buffer layer proceeded for some time, the Kikuchi line were smeared out and broader modulated streaks appeared. This implies that the surface is very rough with multilevel steps of different widths. When at the Bragg point, the reciprocal rods have sharp and bright "nodes", while the reciprocal rods become broader and weaker beyond the Bragg point. This is the reason why the RHEED stripe pattern has a intensity variation in the vertical direction [24]. This reflection pattern also indicates that the Pd buffer layer is single crystal but with high surface roughness.

Elliptical streaks and the Kikuchi lines reappeared after annealing of the Pd buffer layer in Figure 4.4(e), which also denote that the Pd buffer layer has a flat surface and crystalline structure. The RHEED pattern after the growth of FePd was also shown in Figure 4.4(f).

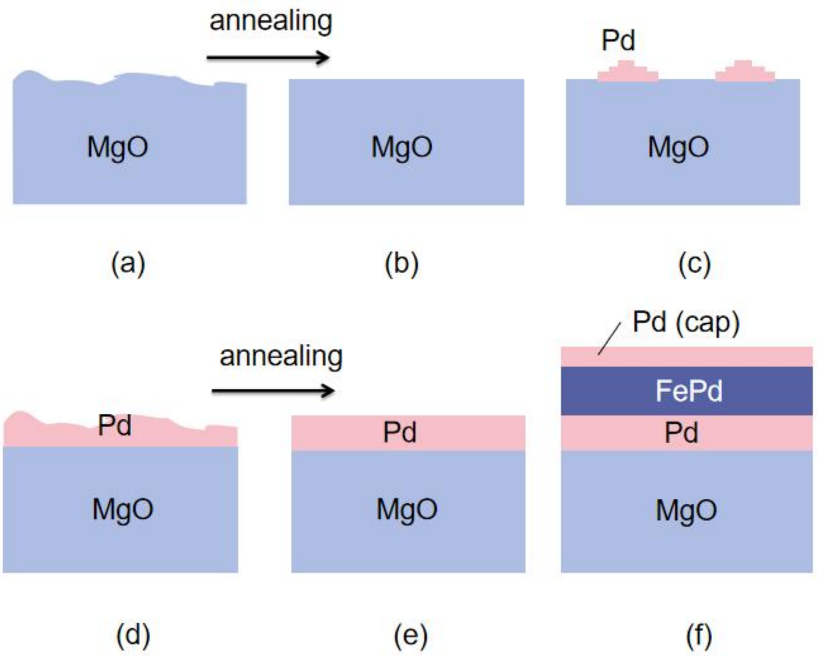

Figure 4.5: Schematic structure diagram of the thin film layer corresponding to the RHEED image.

4.1.4.2 F/S Group

For F/S system, as shown in Figure 4.6(a), the RHEED image of the YBCO surface in (110) crystallographic direction shows some modulated steaks, but there is no Kikuchi line. This indicates that YBCO film is epitaxial by HOPS, but the surface of YBCO is not so flat as the annealed Pd buffer layer in comparison F group.

In addition to the RHEED images, as shown in Figure 4.7(a), SEM images of YBCO can also prove that the YBCO surface is indeed very rough with some spirals, but this is not due to the growth conditions, but rather the growth nature of YBCO. Many thanks to Prof. Dr. Michael Faley for taking these SEM and TEM images.

Figure 4.6(b) shows ring patterns of deposited FePd on YBCO, taken during FePd deposition on YBCO surface. This behavior can be understood as follows. The intensity of Debye rings in the RHEED pattern for sample YBCO/Pd/FePd (sh, RT) is continuously distributed along the circumference. This suggests the random orientation of FePd grains [25]. Therefore, deposited FePd is polycrystalline. As shown in Figure 4.7(b), the TEM images also point out that the FePd is columnarly grown, but oriented along different directions.

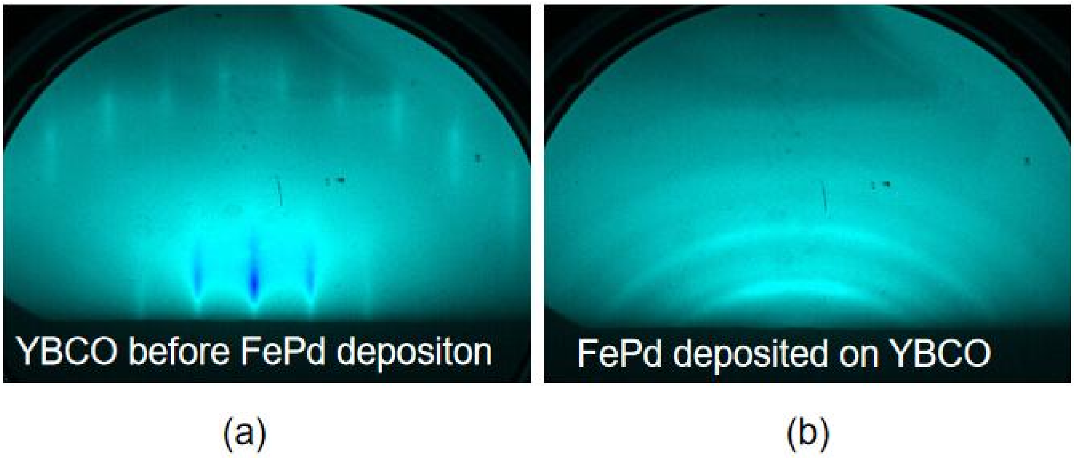

Figure 4.6: RHEED patterns of F/S group in (110) crystallographic direction. (a) RHEED was taken when YBCO was transferred from HOPS to MBE chamber. (b) A ring pattern appeared on the RHEED fluorescent screen, when the deposition of FePd started.

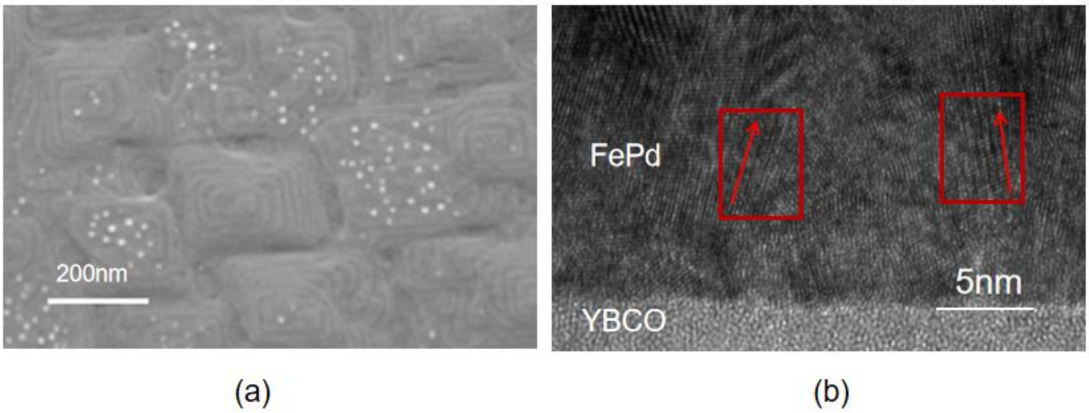

Figure 4.7: (a) SEM image of YBCO, taken by Prof. Dr. Faley.
(b) TEM image of new YBCO/FePd (sh, RT), taken by Prof. Dr. Faley.

4.2 Characterizations with X-ray

The magnetic domain structures and high perpendicular anisotropy of the film are from the presence of the $L1_0$ phase FePd, so XRD can be used to detect the long-range order of this ordered phase within the film.

The measurements are performed on a D-8 diffractometer, whose diffraction vector is always perpendicular to the surface of the sample. Therefore, all the measured parameters are out-of-plane lattice constants.

4.2.1 Comparison F group

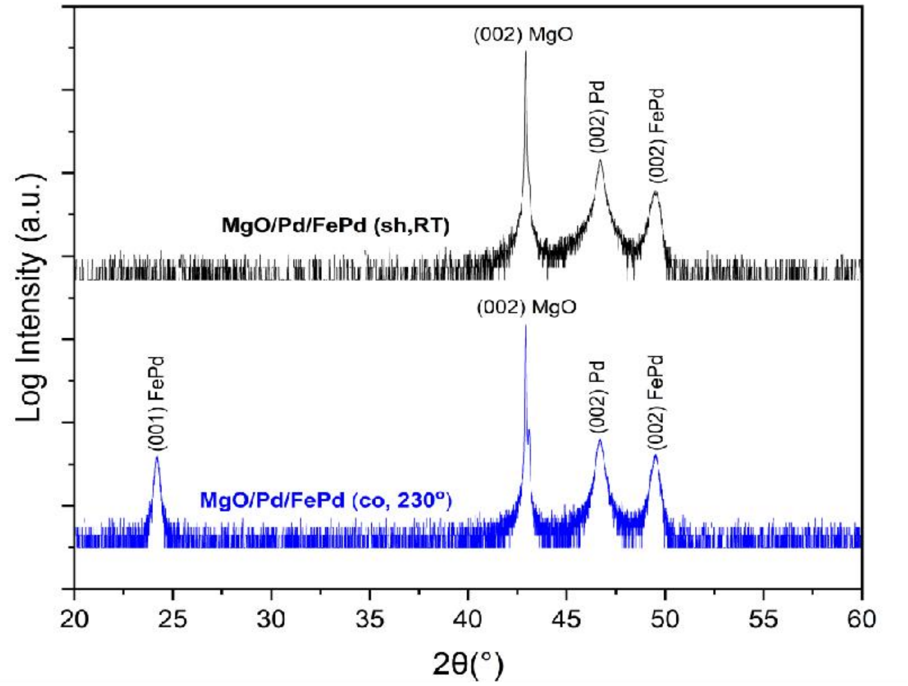

Figure 4.8: X-ray diffraction spectra of comparison F group.

For comparison F group, the XRD patterns are shown in figure 4.8, the calculated lattice constants are shown in the following table 4.3. .The FePd (001) peak represents the superlattice reflection, which comes from an ordered tetragonal distorted crystal structure. The FePd (002) peak represents the fundamental reflection, which comes from a disordered fcc structure [27,28]. Compared to sample MgO/Pd/FePd(sh,RT), the FePd (001) peak disappeared from the XRD pattern of sample MgO/Pd/FePd (co,230℃), which shows that the samples using the co-deposition method have a high long-range order. The higher the integrated intensity of the

FePd (001) peak, the higher the degree of long-range order within the FePd layer and less structural defects.

The lattice constants of FePd (001), FePd (002) and Pd (002) of both comparison F group samples are smaller than the bulk value of the lattice constant of the $L1_0$ phase. This indicates that in the multilayer structure, the lattice constant of the FePd layer in the z-direction becomes smaller, which infers that the lattice constant of FePd in the in-plane becomes larger, thus the FePd layer is in tensile strain.

Table 4.3: Lattice constants calculated from the XRD measurement and corresponding bulk values. [26]

Lattice constant [Å] **sample**	FePd(001)	FePd(002)	MgO(002)	Pd(002)
Bulk value	3.71	3.71	4.21	3.89
MgO/Pd/FePd (co, 230℃)	3.68	3.68	4.21	3.89
MgO/Pd/FePd (sh, RT)	/	3.69	4.21	3.89

4.2.2 F/S group

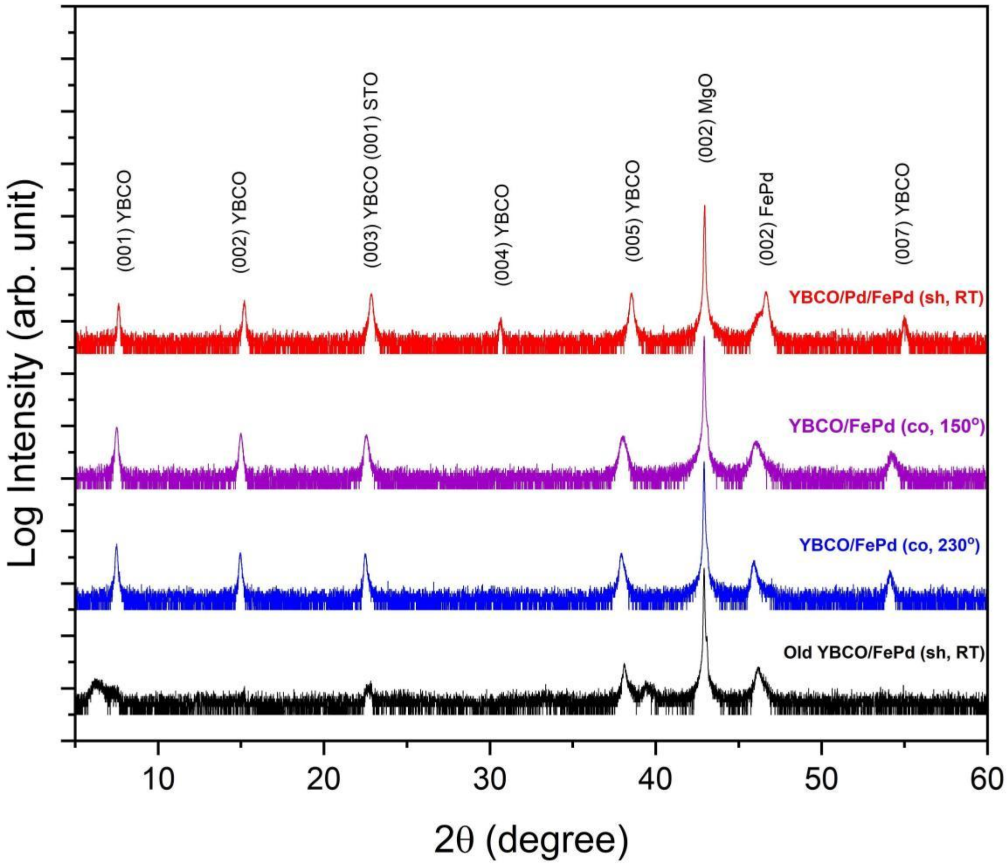

Figure 4.9: X-ray diffraction spectra of F/S group.

For F/S group, the XRD patterns are shown in figure 4.9, the calculated lattice constants are shown in the following table 4.4. As shown in Figure 4.9, the peaks of FePd(001) disappeared in all four samples of the F/S group, which indicates that the samples even using the co-deposition method didn't show any high long-range order. This is consistent with the result that FePd is polycrystalline as shown by the ring pattern in RHEED. Besides, this is also consistent with the TEM image of Fig. 4.7(b) showing the FePd grown in different orientations.

It is obvious that the XRD spectra of the sample Old YBCO/FePd(sh,RT) have some peaks of YBCO with smaller heights or even peaks disappearing directly, which indicates that there is some degradation of YBCO as time goes by.

As the deposition temperature increases from room temperature to 150℃, the peak of YBCO moves to small angle direction, which represents the lattice parameter of YBCO becomes larger in the z-direction, so the strain inside YBCO layer changes from tensile strain to compressive strain. However, the FePd layer is in compressive strain at both room temperature and high temperature.

Table 4.4: Lattice constants of F/S group calculated from the XRD measurement and corresponding bulk values [26].

Lattice constant [Å] **sample**	YBCO(001)	FePd(002)	MgO(002)
Bulk value	11.65	3.71	4.21
YBCO/FePd (co, 150℃)	11.76	3.93	4.21
YBCO/Pd/FePd (sh, RT)	11.59	3.89	4.21

4.3 Surface and magnetic domain characterization

The roughness and topography of the sample can be obtained by atomic force microscopy (AFM), while the out-of-plane magnetic domain structure of the sample can be obtained by magnetic force microscopy (MFM).

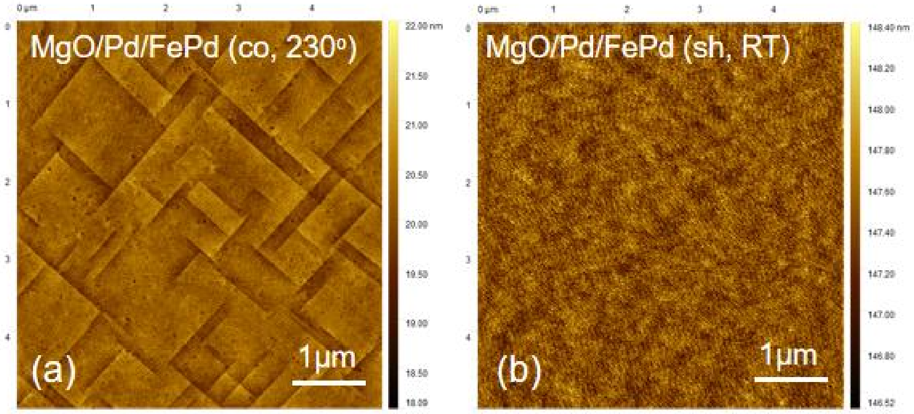

Figure 4.10: AFM images of the comparison F group sample (a) MgO/Pd/FePd (co,230℃) and (b) MgO/Pd/FePd (sh,RT).

4.3.1 Atomic Force Microscopy

For comparison F group, as shown in Figure 4.10(a), a mutually perpendicular terrace structure appeared on the surface of the sample MgO/Pd/FePd (co,230°C) at high deposition temperature. This step structure on the surface may be explained due to plane defects in FePd layer. There is a lattice mismatch between the FePd and Pd layers, so the dislocations inside FePd layer glide along the {111} crystalline plane direction and form steps, thus reducing the stacking fault energy [29]. While the sample (b) MgO/Pd/FePd (sh,RT) grown at room temperature, it has a flatter surface with smaller and more uniform grains. The roughness in Table 4.5 also demonstrates that the surface of the sample at room temperature is smoother.

Table 4.5: Roughness of comparison F group

Sample	MgO/Pd/FePd (co,230℃)	MgO/Pd/FePd (sh,RT)
Deposition T/℃	230	25
roughness/nm	0.386±0.024	0.210±0.004

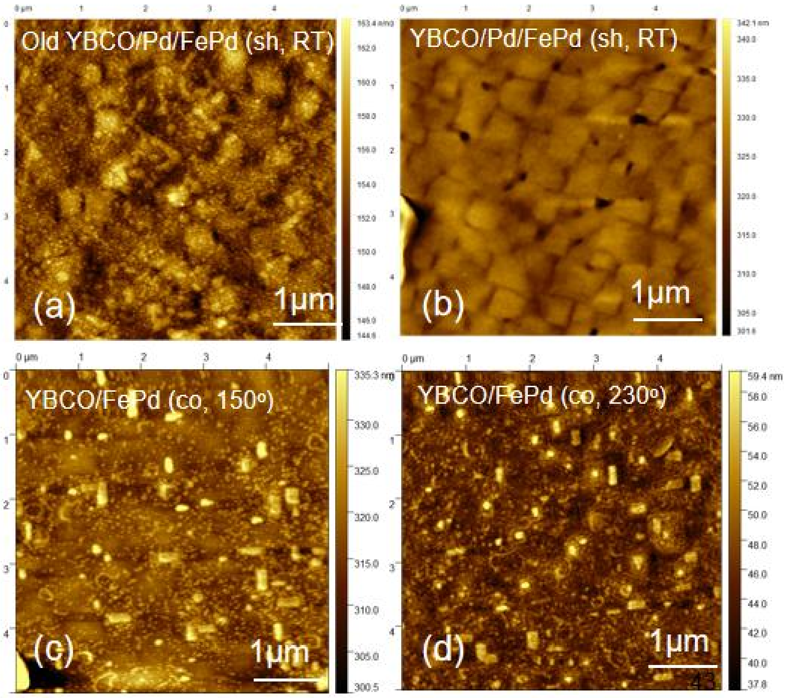

Figure 4.11: AFM images of the F/S group sample

For the samples in the F/S group in Figure 4.11, the surface of the samples (a) and (b) grown through shuttered deposition at room temperature had rough surfaces and showed voids and holes on the surface. However, the samples (c) and (d) which were grown at high temperature have smooth surfaces and small grains. Further, as the deposition temperature increases from 150℃ to 230℃, the surface turns to be smoother which is shown in Table 4.6 and by comparing Figure 4.11(c) and (d), the higher the deposition temperature, the smoother the surface.

Table 4.6: Roughness of F/S group.

Sample	Deposition T/℃	Roughness/nm
(a)Old YBCO/Pd/FePd (sh,RT)	25	3.050±0.358
(b)YBCO/Pd/FePd (sh, RT)	25	3.831±0.519
(c)YBCO/FePd (co,150°C)	150	4.267±0.844
(d)YBCO/FePd (co,230°C)	230	3.124±0.267

4.3.2 Magnetic Force Microscopy and Hysteresis Loop

The method magnetic force microscopy or MFM is the main method of scanning probe microscopy to probe samples with magnetic properties or magnetic materials and elucidate features such as magnetic domains and domain walls in a sample. This method is widely used in the field of magnetic storage media for quality control. The SQUID M-H hysteresis loops were measured using Quantum Design's MPMS system at magnetic fields parallel and perpendicular to the sample surface, with magnetic fields up to 5 T in the measurement.

4.3.2.1 Comparison F Group

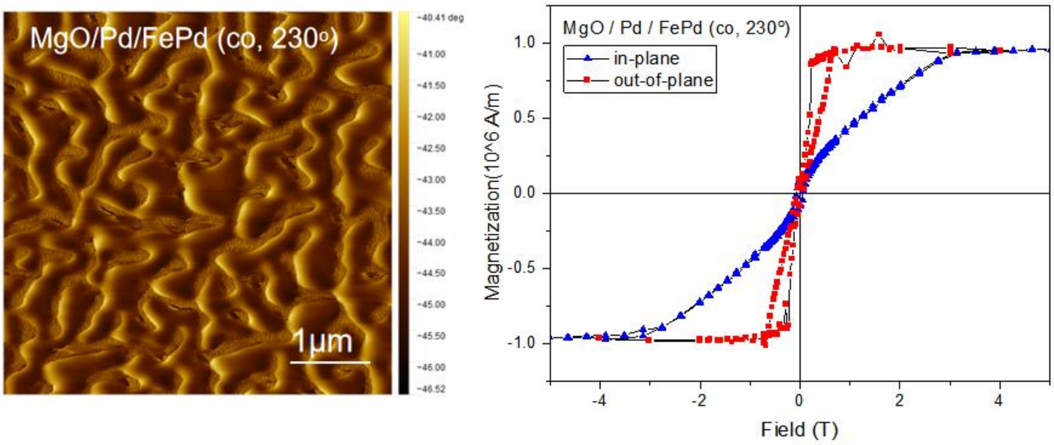

Figure 4.12: MFM image of sample MgO/Pd/FePd(co,230℃) and its Magnetization vs. Applied field (M-H) curve.

For comparison F group, MFM image of the sample with co-deposition and high deposition temperature shows a very clear maze pattern of magnetic domains as shown in left side of Figure 4.12. From Figure 4.12 right, easy magnetization axis of the thin film is in out-of-plane direction and this also means that sample MgO/Pd/FePd (co,230 ℃) has high perpendicular magnetic Anisotropy (high PMA).

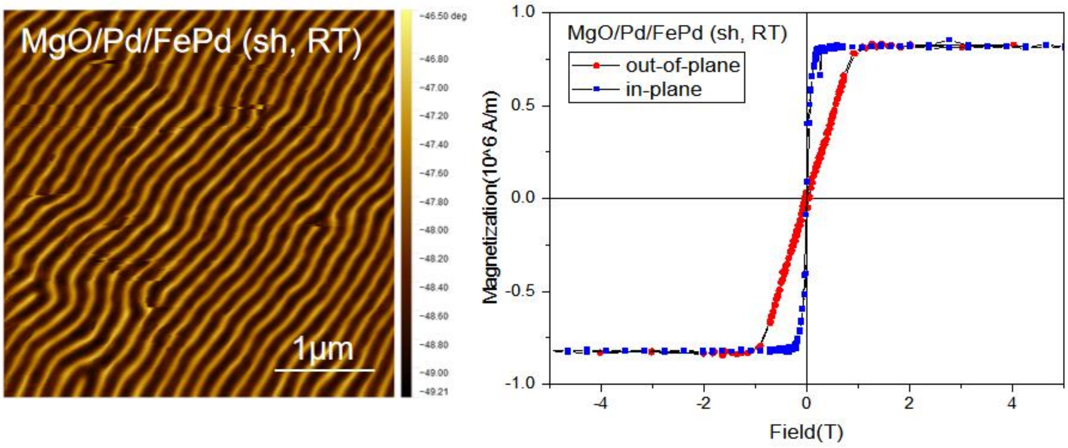

Figure 4.13:MFM image and M-H curve of sample MgO/Pd/FePd(sh,RT) .

For the sample grown in room temperature, MFM image shows a striped magnetic domain pattern. From M-H curve of Figure 4.13, easy magnetization axis of the thin film is in in-plane direction and this also represents that sample MgO/Pd/FePd (sh,RT) has low perpendicular magnetic Anisotropy (low PMA). Besides, a striped domain pattern here represents not just in-plane domains, but a mixture of in-plane and out-of-plane domains.

4.3.2.2 F/S Group

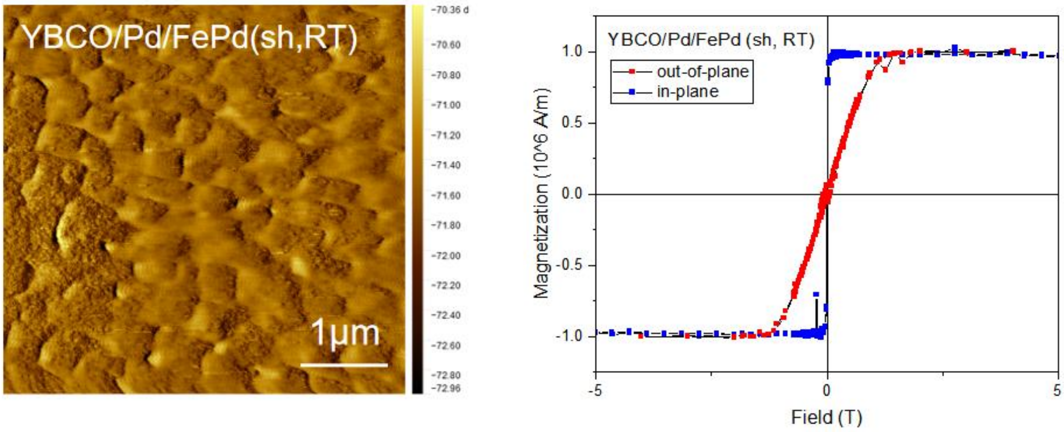

Figure 4.14: MFM image and M-H curve of sample YBCO/Pd/FePd(sh,RT) .

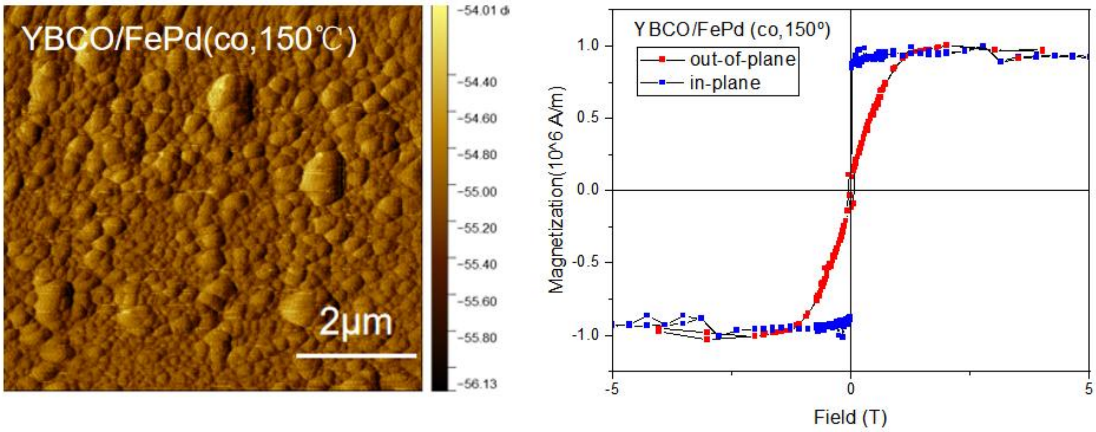

Figure 4.15: MFM image and M-H curve of sample YBCO/FePd(co,150℃) .

For F/S group, the four samples didn't show any domain pattern from MFM images. One possible reason for this is that in these two samples in F/S group, there are only in-plane magnetic domains, so the MFM cannot scan any magnetic domain patterns. However, M-H curves of sample YBCO/Pd/FePd (sh,RT) and YBCO/FePd (co,150℃) indicate that both easy magnetization axis are in in-plane direction.

Here, the reason for discarding the other two samples in F/S group is that the superconducting layer of sample old YBCO/FePd (sh,RT) has degraded YBCO layer and the deposition temperature of sample YBCO/FePd (co,230 ℃) is too high, resulting in the loss of oxygen in YBCO, structural changes and then superconductivity is broken.

4.4 Temperature Dependence of the Resistance

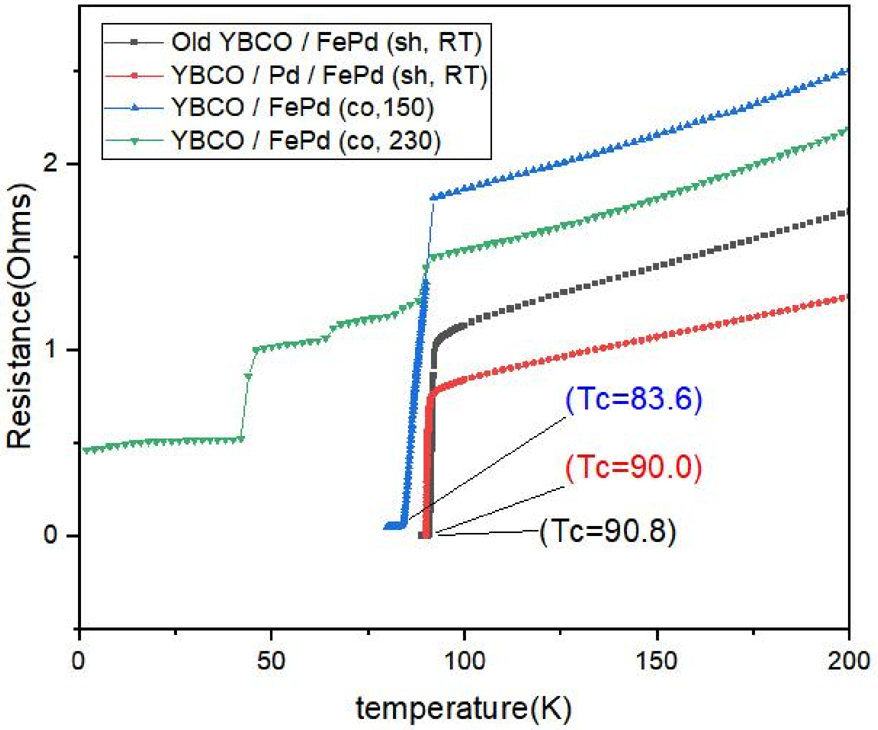

Figure 4.16: Resistance vs. Temperature curves of F/S group.

As shown in Figure 4.16, the green Resistance vs. Temperature (R-T) curve is notable and unusual. The transition of this sample YBCO/FePd (co,230 ℃) was broken into three parts, which represents the complete superconductivity is broken. The reason is that YBCO will lose oxygen in high temperature and ultra-high vacuum conditions, which leads to the degradation of YBCO.

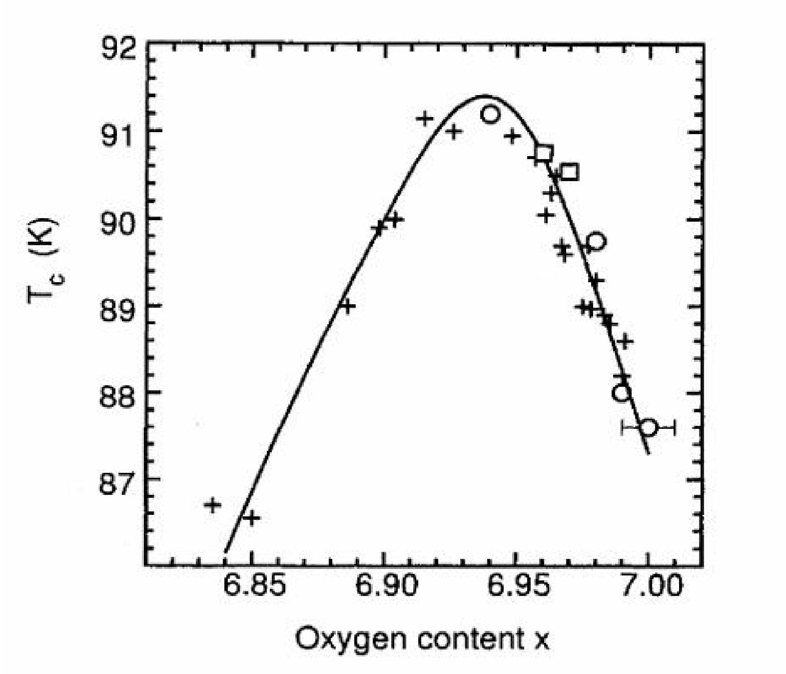

Figure 4.17: Tc as determined from the midpoint of the diamagnetic transition of $YBa_2Cu_3O_x$ in 1 G (parallel to ab plane), vs oxygen concentration x. This figure is taken from [30].

Figure 4.17 displays T_c vs oxygen concentration. A moderate decrease in oxygen content leads to a higher T_c, which explains why sample Old YBCO/FePd (sh,RT) (a sample with a slightly degraded YBCO) has a 0.8K higher T_c than sample YBCO/Pd/FePd (sh,RT). Compared to sample YBCO/Pd/FePd (sh,RT), sample YBCO/FePd (co,150 ℃) loses oxygen substantially at the high temperature of 150 degrees, which leads to a significant drop in T_c from about 90K to 83.6 K.

5 Summary

This project is a supplementary study on superconductor-ferromagnet ($YBa_2Cu_3O_{7-x}$-FePd) heterostructures in Dr. Annika Stellhorn's PhD and Msc. Jianwei Ye's master thesis, in which FePd thin films could be grown with equivalent qualities without the Cr seed layer between MgO substrate and Pd buffer layer. FePd thin films with various PMA have been grown with excellent quality by using co-deposition and shuttered growth methods on low-temperature superconductor Nb.

In this project, we have grown FePd ferromagnetic films on $YBa_2Cu_3O_{7-x}$ high-temperature superconducting thin films. Furthermore, FePd was deposited on the MgO substrate as a comparison group.

In the HOPS system, a 60 nm YBCO superconducting film was prepared by Prof. Dr. Michael Faley on a MgO substrate with a film T_c of about 90K. Immediately afterwards, the sample was transferred to an OMBE chamber and then FePd was deposited with both co-deposition and shuttered deposition methods on the YBCO superconducting film .

The in-situ characterization method RHEED was used to monitor the growth process during the deposition. From the results of RHEED image analysis, it appears that YBCO prepared with HOPS is a single crystal with a rough surface, which is due to the nature of YBCO spiral growth. But when deposition of FePd started, the samples changed directly to polycrystalline. However, all samples of the comparison F group were single crystals with flat surfaces due to annealing of the substrate and Pd buffer layer, which resulted in a good precondition for FePd deposition.

Combining the MFM images and M-H curves it can be concluded that

(i) In the comparison F group, FePd grown by high temperature (230℃) co-deposition on Pd buffer layer and MgO substrate has high PMA. The high PMA sample shows a clear maze pattern in the MFM image. However, sample FePd/Pd/MgO(sh,RT) with low PMA grown in room temperature by the shuttered deposition shows a streak pattern in the MFM image.

(ii) However, in the F/S group, none of the four samples were detected with any magnetic domain pattern, but they are all low PMA samples as known from the M-H curves. This may be due to the fact that the samples only have in-plane magnetic domain structure, while MFM can only get information of out-of-plane magnetic domain structure.

The superconducting properties of YBCO were investigated by resistance-temperature measurements. The results show that higher FePd deposition temperature and vacuum leads to the degraded YBCO. This is because YBCO loses oxygen when it is in vacuum and high temperature. However, if FePd is deposited at a lower temperature, FePd will become polycrystalline, and if FePd is deposited under low temperature and oxygen conditions, FePd will be oxidized. Therefore, due to the different growth conditions of FePd and YBCO, it is very difficult to make FePd perfectly deposited on YBCO as a single crystal.

6 Outlook

For the problem of FePd to be deposited single crystalline on YBCO, several solutions are proposed in the following outlook.

Since FePd did not grow epitaxially on YBCO at room temperature, longer deposition and diffusion times were considered to obtain a more uniform and ordered $L1_0$-phase. In addition, contamination and degradation of YBCO during the transfer process can be avoided by using a vacuum transfer chamber.

In the next study, the correlation between resistance and magnetization at different temperatures will first be investigated. R-H, M-H in different temperatures around T_c.

For the case where the F/S group does not have any magnetic domain pattern, the in-plane tip can be used to analyse the in-plane domain structure, which can further confirm whether the F/S group samples have in-plane magnetic domains.

Since Fe can react with oxygen, the interface between FePd and YBCO of sample FePd/Pd/YBCO(sh,RT) needs to be further analyzed and more information about the interface can be obtained by using EDX.

References:

[1] Annika Stellhorn, Tailoring superconducting states in superconductor -ferromagnet hybrids, New J. Phys. 22 (2020) 093001, doi: 10.1088/1367-2630/abaa02.

[2] Zhaorong Yang, Martin Lange, Alexander Volodin, Ritta Szymczak and Victor V. Moshchalkov, "Domain-wall superconductivity in superconductor–ferromagnet hybrids", Nature materials, Vol.3 (Nov.2004). doi:10.1038/nmat1222.

[3] Matthias Eschrig, Spin-polarized supercurrents for spintronics, Physics Today 64(1), 43 (2011); doi: 10.1063/1.3541944

[4] V. Gehanno and A. Marty, B. Gilles, Y. Samson. Magnetic domains in epitaxial ordered FePd(001) thin films with perpendicular magnetic anisotropy. Physical Review B,Vol.55(18), pp: 12552-12555.

[5] Kittel, C. Introduction to Solid State Physics (John Wiley & Sons, Inc., New York, 1986), 6th edn.

[6] M. T. Johnson, P. J. H. Bloemen, F. J. A. den Broeder, and J. J. de Vries. "Magnetic anisotropy in metallic multilayers". Reports on Progress in Physics, 59(11) (Nov.1996), pp. 1409 – 1458. doi: 10.1088/0034-4885/59/11/002.

[7] Callen, E. & Callen, H. B. Magnetostriction, forced magnetostriction, and anomalous thermal expansion in ferromagnets. Physical Review 139, A455(1965).

[8] V. V. Schmidt, "The Physics of Superconductors: introduction to fundamentals and applications", Springer-Verlag Berlin Heidelberg New York in 1997, DOI 10.1007/978-3-662-03501-6.

[9] Annette Bussmann-Holder and Hugo Keller, "High-temperature superconductors: underlying physics and applications", De Gruyter, 2019, pp.1-12. doi:10.1515/znb-2019-0103.

[10] Matthias Eschrig, "Spin-polarized supercurrents for spintronics", Physics Today 64, 1, 43 (2011); doi: 10.1063/1.3541944.

[11] Chris Safranski, "Resistance of the Superconducting Material YBCO", a Senior Project, California Polytechnic State University.

[12] J. Reichow. Technical System Description of DCA MBE M600 Molecular Beam Epitaxy System. Jan. 2010.

[13] Jinkwan Kwoen and Yasuhiko Arakawa. "Classification of Reflection High-Energy Electron Diffraction Pattern Using Machine Learning", Crystal Growth and Design, 20(8), 2020, pp: 5289-5293. doi: 10.1021/acs.cgd.0c00506.

[14] Sakamoto, T. “Rheed Oscillations in MBE and Their Applications to Precisely Controlled Crystal Growth”. In: Dhez, P, Weisbuch, C. Physics, Fabrication, and Applications of Multilayered Structures. Springer, Boston, MA. doi: 10.1007/978-1-4757-0091-6_5.

[15] A. Glavic. “Multiferroicity in oxide thin films and heterostructures”. PhD thesis. RWTH Aachen University, 201.

[16] Gustavo Cordova, Brenda Yasie Lee and Zoya Leonenko. “Magnetic Force Microscopy for Nanoparticle Characterization”. Nano World Journal, January 2016, doi: 10.17756/nwj.2016-022.

[17] R. L. Fagaly. “Superconducting quantum interference device instruments and applications”. Review of Scientific Instruments, 77, 101101 (2006). doi: 10.1063/1.2354545.

[18] P. J. Zakalek, T. Brückel, and L. Juschkin. “Magnetic interface effects in thin film heterostructures”. PhD thesis, Universitäts -bibliothek der RWTH Aachen, 2015.

[19] Y. Kinoshita, T. Miyakawa, X. Xu. “Long-distance polarizing microscope system combined with solenoid-type magnet for microscopy and simultaneous measurement of physical parameters”. Rev. Sci. Instrum. 93, 073702 (2022); doi: 10.1063/5.0094747.

[20] CrysTec. Data-Sheet of MgO substrate.

[21] Jianwei Ye, Investigation of the Domain Structure of FePd Thin Film. RWTH Aachen University, 2020.

[22] Michael Faley, “Variation of the oxygen content in $YBa_2Cu_3O_{7-x}$ films deposited by high oxygen pressure DC-sputtering”. IEEE Transactions on Appled superconductivity, 3(1), 03, 1993.

[23] Michael Faley, “Multilayer buffer for high-temperature superconductor devices on MgO”. Applied Physics Letters 89, 082507(2006).

[24] Shuji Hasegawa, “Reflection high-energy electron diffraction”. Characterization of Materials, pp: 1925-1938, 2012.

[25] V. V. Balashev and V. V. Korobtsov, “Structure of Ultrathin Polycrystalline Iron Films Grown on SiO2/Si(001)”. Technical Physics, vol.63(1), pp: 73 – 77, 2018.

[26] T. Ichitsubo and K. Tanaka. “ Single-crystal elastic constants of disordered and ordered FePd” . In: Journal of Applied Physics 96.11 (Dec. 2004), pp. 6220 – 6223. doi: 10.1063/1.1809775

[27] V. Gehanno, “Perpendicular magnetic anisotropy of epitaxial thin films of FePd ordered alloys,” Ph.D. dissertation, Universit´e JoSeph-Fourier - Grenoble I, 1997.
[28] B. E. Warren, X-ray Diffraction: by B. E. Warren. Addison-Wesley Pub. Co,1969.
[29] D. Halley, Y. Samson, A. Marty, C. Beign, and B. Gilles. “Surface morphology and chemical ordering in FePd/Pd(001) thin layers”. In: Surface Science 481.1-3 (June 2001), pp. 25 – 32. doi:10.1016/s0039-6028(01)01061-5.
[30] V. Breit, P. Schweiss, R.Hauff, H.Wuehl, etc. “Evidence for chain superconductivity in near-stoichiometric $YBa_2Cu_3O_x$ single crystals”. Physical Review B Vol.52.22, (Dec.1995), pp. 727-730.
[31] Fernando Rinaldi, “Basics of Molecular Beam Epitaxy (MBE)”. Annual Report 2002, Optoelectronics Department, University of Ulm.

7 Acknowledgement

I finished this thesis at JCNS-2 / PGI-4/ PGI-5 in Forschungszentrum Jülich (FZJ) during the last 9 months. I would like to sincerely thank all my colleagues and supervisors who have helped and supported me.

Many thanks to Prof. Dr. Thomas Brückel for providing me this wonderful opportunity to work at JCNS-2 and supporting my work.

Many thanks to Prof. Dr. Joachim Mayer for reviewing my thesis as the examiner.

Many thanks to Dr. Emmanuel Kentzinger, Dr. Connie Bednarski-Meinke, Prof. Dr. Michael Faley, Dr. Mai Hussein and Vitor Alexandre, de Oliveira Lima for all the support, discussions and many useful suggestions every weeks.

Many thanks to Dr. Emmanuel Kentzinger, Dr. Connie Bednarski-Meinke, Dr. Mai Hussein and Vitor Alexandre, de Oliveira Lima for your careful revision of my paper.

Many thanks to Dr. Connie Bednarski-Meinke for help and patience with operation of AFM, MFM and OMBE.

Many thanks to Prof. Dr. Michael Faley for perparing all YBCO samples and taking SEM, TEM images to support our work.

Many thanks to Dr. Annika Stellhorn and Msc. Jianwei Ye for providing her/his experience and lots of suggestions on optimized growth parameters of the OMBE system.

Many thanks to PD Dr. Oleg Petracic, Dr. Shibabrata Nandi and Dr. Ulrich Rücker for the safety instructions on the MPMS system, the PPMS system and the X-ray lab.

Many thanks to Berthold Schmitz for helping me solve problems in using the PPMS, MPMS and DynaCool systems.

Many thanks to Dr. Lei Cao, Yifan Xu and Chenyang Yin for teaching me deal with the XRR data and the operation of the XRD instrument.

At last I would like to especially thank my parents and friends for their love and support.